Structural Durability & Health Monitoring

Tech Science Press

https://doi.org/10.32604/sdhm.2026.074828

ARTICLE

Design and Modeling of Novel Wind Turbine Structures Incorporating Nanocomposite Materials

Mohammed Yahya[1,*], Safaaldeen A. Sulyman[2], Joban Sahota[1], Gursingh Aikum Dhugga[1] and Saiakash Shunmugavel[1]

[1]Mechanical Engineering, Toronto Metropolitan University, Toronto, ON, Canada
[2]College of Basic Education, Mosul University, Mosul, Iraq

*Corresponding Author: Mohammed Yahya. Email: mohammed.yahya@torontomu.ca

Received: 19 October 2025; Accepted: 26 January 2026; Published: 18 May 2026

ABSTRACT: The structural integrity and longevity of wind turbine blades are critical determinants of the efficiency and reliability of wind energy systems. As the primary components responsible for converting kinetic wind energy into mechanical torque and subsequently electrical power, the aerodynamic, structural, and material characteristics of rotor blades directly influence turbine performance and operational lifespan. This research addresses the limitations of conventional blade designs, often characterized by stress concentration, fatigue damage, and dynamic instability by introducing a novel diamond-lattice internal support structure aimed at improving mechanical strength, fatigue resistance, and dynamic stability. Finite element simulations performed in COMSOL Multiphysics® were used to evaluate the proposed configuration against a traditional X-shaped design under realistic aerodynamic and gravitational loading. The results reveal that the proposed structure reduced peak stress concentrations by 11.38%, achieves a 15.39% reduction in volumetric elastic strain, and improves fatigue performance by 14.38% while significantly enhancing stiffness and buckling resistance without adding substantial mass. To assess dynamic performance, a Campbell diagram analysis was conducted, confirming that no resonance intersections occur between the excitation harmonics and the natural frequency modes within the operational speed range. This finding indicates that the blade operates safely below critical resonance thresholds and benefits from centrifugal stiffening, which further improves stability at higher rotational speeds. Moreover, the incorporation of carbon nanotube (CNT), nano-silica, and hybrid nanocomposite reinforcements into the composite matrix enhanced stiffness, vibration damping, and crack resistance, yielding superior fatigue and vibration behavior. Overall, the combined application of structural innovation and nanomaterial enhancement offers a promising pathway toward the development of lighter, stronger, and dynamically stable wind turbine blades, contributing to improved performance, reliability, and sustainability in modern renewable energy systems.

KEYWORDS: Wind turbine; turbine blades; aerodynamics; numerical modeling

1 Introduction

Wind energy has grown into a vital component of the global renewable energy strategy. Its development has been driven by the increasing demand for clean, sustainable power and the urgent need to reduce environmental impact, making it a key pillar in the transition to low-carbon energy systems. Wind turbines represent the primary technology for harnessing wind power, with origins in Professor James Blyth's pioneering development of Britain's first electricity-generating wind turbine in July 1887 [1]. Wind turbines rely fundamentally on rotor blade performance. The blades convert kinetic wind energy into mechanical torque,

subsequently transformed into electrical energy [2]. Wind turbine efficiency, durability, and operational lifespan are thus intimately tied to blade mechanical, structural, and material properties [3].

The design of wind turbine blades represents a critical trade-off between aerodynamic performance and structural strength. Aerodynamic factors predominantly influence the outer two-thirds of the blade span, where optimizing lift and minimizing drag are essential for energy capture. In contrast, the inner one-third of the blade is primarily governed by structural requirements due to the elevated bending moments and shear forces experienced near the root. Modern blades are typically constructed as hollow composite structures composed of two aerodynamic shells [4,5], one on the suction side and one on the pressure side. The load-carrying shells are internally connected by one or more structural shear webs, which utilize to transfer shear forces and enhance the overall rigidity of the blade. Conventional blade configurations typically incorporate one or two internal shear webs oriented approximately perpendicular to the chord line, providing essential structural reinforcement, as illustrated in Fig. 1 [6].

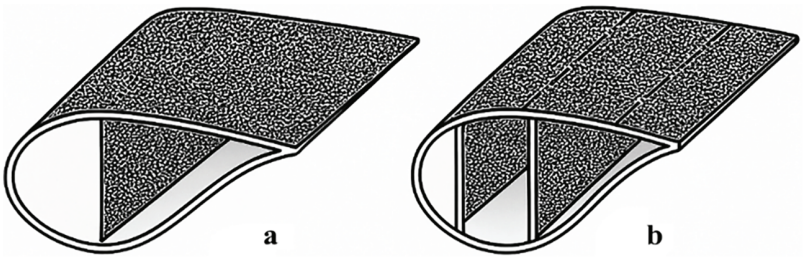

Figure 1: Sketch of a blade concept: (**a**) Blade design with one shear web. (**b**) Blade designs with two shear webs.

In early-generation wind turbine blades, structural loads were primarily carried by a central box girder. However, over the past decade, this configuration has been largely supplanted by load-bearing shell structures reinforced with spar caps, as illustrated in Fig. 2. This design has become the prevailing standard in modern blade architecture.

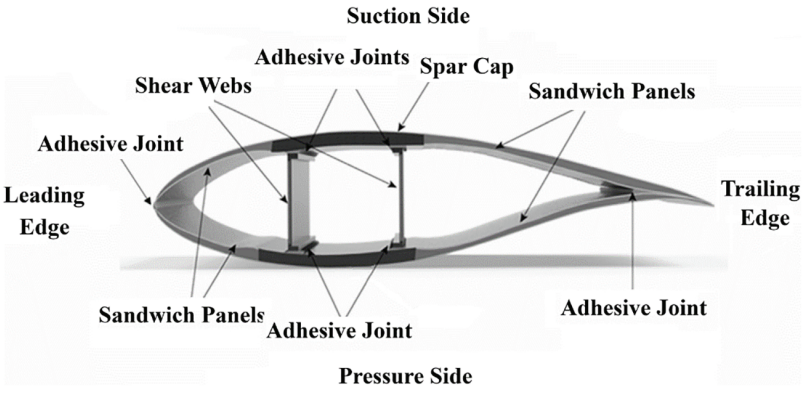

Figure 2: Cross-sectional schematic of a composite wind turbine blade showing the suction/pressure sides, sandwich panels, spar cap, shear webs, and adhesive joints that form the internal load-carrying structure.

Contemporary wind turbine blades typically incorporate one to three internal shear webs, depending on structural and aerodynamic requirements, with spar caps providing longitudinal stiffness and strength. The blades are also tapered and twisted along their span: tapering reduces material usage and manufacturing cost while accommodating the progressively higher structural loads from tip to root. In parallel, spanwise twist enhances aerodynamic efficiency by maintaining favorable angles of attack, increasing lift, and reducing

drag near the high-velocity tip region [6]. Schubel and Crossley [7] present key principles and challenges in modern horizontal-axis wind turbine (HAWT) blade design, which dominates the industry for its efficiency and controllability. The study discusses Lift-based blades, typically three-bladed, offer the best balance of performance, cost, and aesthetics. The finding of this study highlights the key design factors include tip speed ratio, aerofoil selection, blade planform, structural loads, and material choices, with blades optimized differently at the root, mid-span, and tip. Balat [8] reviewed modern wind turbine technology, highlighting advances that have made wind energy a mature, efficient, and cost-competitive renewable source. The study discusses horizontal and vertical-axis designs, aerodynamic blade optimization, control systems, and the shift to larger, more reliable turbines. Key developments include improved materials, electronics, and pitch control strategies, which enhance efficiency and grid integration. Rehman et al. [9] provided a comprehensive review of HAWT blade design methodologies aimed at enhancing efficiency. Their work surveyed experimental, numerical, and theoretical approaches to blade optimization, including techniques to reduce cut-in speed, mitigate flow separation, and improve structural and aerodynamic performance using both passive and active control devices, as well as advanced materials and scaled testing methods. Martulli et al. [10] conducted a critical review of wind turbine blade designs and materials, focusing on their impact on end-of-life management. They highlighted how the prevalent use of fibre-reinforced composites, thermoset resins, adhesives, and large monolithic structures hinders recycling and sustainable disposal. The review also examined strategies to improve wind turbine blades sustainability, including life extension, structural health monitoring, and designing for enhanced recyclability. Richards et al. [11] presented an aeroelastic design strategy for large wind turbine blades that incorporates damage tolerance considerations, focusing on trailing-edge bond line failures. Their study of wind turbine blade demonstrated that using flat-back airfoils improves structural efficiency, fatigue performance, and damage tolerance, enabling more slender and cost-effective designs. They emphasized the importance of integrating aeroelastic performance and reliability goals early in the design process to reduce maintenance costs and enhance offshore wind turbine competitiveness. Wu et al. [12] proposed a multi-objective optimization framework for wind turbine blade design that simultaneously improves power output, reduces structural loads, and mitigates stall risk. Using a genetic algorithm and parametric modeling, they demonstrated wind turbine blade optimization, power, reduction in root bending moment, and improved stall performance through a novel stall risk assessment method and optimal tip-speed-ratio control. de Almeida et al. [13] conducted a comprehensive structural analysis of a DTU 10-MW offshore wind turbine blade by comparing geometrically nonlinear beam and layered shell finite element models. Their study highlighted the effectiveness of the Timoshenko beam model in capturing global blade behavior under extreme loads, while also emphasizing the necessity of shell models for accurately predicting local instability phenomena such as trailing edge buckling. Zhu et al. [14] provided a comprehensive overview of wind energy science and engineering, identifying key research challenges in aerodynamics, materials, structural dynamics, controls, and grid integration. The paper highlights the need for multidisciplinary approaches to enable continued growth and innovation in wind turbine technology.

Agarwala and Chin [15] present a structurally compliant redesign of a 5 MW wind turbine blade aimed at improving aerodynamic efficiency and reducing mass. The redesigned blade features two inner blades with a thinner root airfoil and a dual-spar structure to enhance stiffness and aerodynamic performance using iterative finite element analysis. Results demonstrate that the redesigned blade is both lighter and structurally sound, offering potential benefits for load control and turbine scalability.

Taima et al. [16] analyzed the dynamic stability of rotating tapered 2D FGM beams using Floquet theory. The study highlights key effects of rotation, taper, and material gradients on subharmonic instability. Capuzzi, et al. [17] propose an aeroelastically tailored wind turbine blade that uses bend-twist coupling for passive load adaptation. The design employs tow steered composites and a curved planform to achieve controlled elastic

twist under flapwise loading, enhancing power capture and reducing gust loads. A finite element model confirms the targeted twist distribution and structural integrity under extreme loads. Modal analysis shows no resonance, and nonlinear effects slightly stiffen the response without impacting performance. Migliaccio et al. [18] developed a nonlinear beam theory model for rotor blades, accounting for curvature, twist, taper, and large deflections. The model captures both geometric and material nonlinearities and is validated against finite element results. It offers an efficient, accurate alternative to full 3D analysis for blade-like structures with complex deformation behavior.

Several studies employing Computational Fluid Dynamics (CFD) have demonstrated that variations in blade taper can significantly influence aerodynamic performance. These numerical investigations consistently highlight that optimized taper distributions contribute to improved lift characteristics, reduced drag, and enhanced overall aerodynamic efficiency. Such findings reinforce the importance of taper optimization as a key design parameter in the development of high-performance wind turbine blades. In addition to aerodynamic considerations, the structural literature emphasizes that the primary stresses experienced by wind turbine blades arise from a combination of bending and shear loads. These stresses develop under the simultaneous action of aerodynamic forces, centrifugal effects, and gravitational loading, all of which contribute to the complex stress environment encountered during rotational operation [4,19]. Understanding the interplay between these load components is therefore essential for ensuring structural integrity, fatigue resistance, and long-term reliability in modern utility-scale blade designs.

Recent developments in wind turbine blade design have increasingly focused on the optimization of internal support structures mitigate persistent structural challenges. Current conventional utility-scale wind turbine blades typically employ two or more internal shear webs oriented perpendicular to the chord axis, serving as primary load-bearing components [6,20].

The two-shear-web design structure provides multiple benefits for structural performance and manufacturing procedures. The straightforward nature of its design results in simpler fabrication while decreasing production expenses as per Brondsted et al. [6]. The design configuration successfully transfers loads through efficient channels so the blade root receives aerodynamic forces, which help resist flapwise and edgewise bending moments according to Manwell et al. [20]. Weight optimization in the design occurs through its minimal component usage to achieve both improved aerodynamic performance and decreased material expenses and transportation costs, as described in [19]. Large blade formats and high loading scenarios may cause the design to buckle because insufficient stiffeners make thin wall sections structurally unstable [21,22].

While this configuration offers baseline structural reinforcement, it remains susceptible to significant stress concentrations, particularly at the blade root, spar caps, and along the leading and trailing edges. These localized stress regions are critical sites for the initiation of fatigue damage, material degradation, and eventual structural failure. Stress concentrations in these areas are exacerbated under dynamic loading conditions, contributing to premature fatigue life reduction and increasing the likelihood of delamination and buckling. These phenomena not only compromise the structural integrity of the blade but also reduce its operational lifespan and increase maintenance demands. To address these limitations, contemporary research has explored a variety of structural innovations. These include the implementation of alternative shear web configurations (e.g., multi-web and box-beam layouts) [23].

New invention implements of Cross-Sectional Shear Distortion (CSSD) reinforcement between two shear webs to stop transverse shear distortion. The internal geometry receives its connection through wire/pin or dry fiber mat solutions, as shown in Fig. 3 [6,23]. The method positions tension-bearing diagonal members to stop in-plane deforming actions, which could cause panel failure.

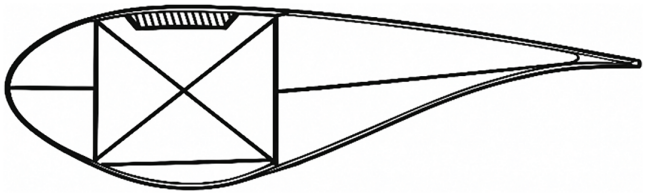

Figure 3: Sketch of Cross-Sectional Shear Distortion (CSSD).

The wire or pin solution shown in Fig. 3, employs tensile elements such as wires, metallic pins or dry fiber mat solution, placed diagonally across which form a diagonal "X" pattern inside the blade's internal structures. The spacing between these elements follows a regular pattern between two to five meters based on how the blade loads are distributed and the structural demands function. Under combined flapwise and edgewise loading, the diagonal components resist axial tension to stabilize the internal geometry and minimize shear web displacement, which improves cross-sectional strength. The blade internal structure benefits from enhanced geometric stability because of shear cross reinforcements, which the elements create restrained movements between essential internal components, which lead to the significant reduction of cross-sectional deformations [23,24]. The reinforcement system relies primarily on axial tension to maximize structural stiffness while minimizing material usage. This design approach is consistent with established wind turbine blade engineering practice, where tension-dominated load paths, particularly in carbon-fiber spar caps and primary load-bearing elements, are favored due to their high stiffness-to-weight efficiency, improved fatigue performance, and structural reliability under cyclic operational loading conditions [25,26].

Recent advances in wind turbine blade design have significantly improved aerodynamic efficiency and structural performance through optimized taper and twist distributions, aeroelastic coupling, and the use of advanced composite materials. These developments have enabled the production of longer and lighter blades while maintaining acceptable stiffness and cost efficiency. However, despite these improvements, commercial blades continue to face critical challenges, including localized stress concentrations, fatigue-induced delamination, and limited resistance to buckling under large-scale and cyclic loading conditions. Conventional internal configurations based on shear webs and spar caps, although effective under moderate loads, often lack the stiffness and fatigue endurance required for modern utility-scale turbines.

To address these limitations, this study proposes a novel internal diamond-lattice reinforcement concept integrated with nano-enhanced composite materials. The proposed configuration aims to improve load redistribution, enhance fatigue life, and increase buckling resistance without compromising manufacturability or weight efficiency, thereby providing a structurally robust solution for next-generation wind turbine blades.

2 Theory and Background

2.1 One-Dimensional Momentum Theory

Wind turbine performance is fundamentally governed by wind characteristics, as the power extracted from the wind scales with the cube of the wind speed ($P \propto AU^3$), where P is the extracted power, U is the wind speed, and A is the rotor swept area. This cubic dependence implies that even small variations in wind speed can result in significant changes in power output, underscoring the importance of accurately understanding wind dynamics in efficient turbine design.

Since wind speed varies significantly with both height and time, turbine blades must be designed to withstand unsteady and dynamic aerodynamic loads. A foundational theoretical model used to estimate the power potential of an ideal wind turbine rotor was proposed by Betz in 1926 [20].

This simplified model is based on linear momentum theory, originally developed over a century ago for the performance prediction of marine propellers. The analysis considers a control volume bounded by the surface of a stream tube and two cross-sectional planes, as illustrated in Fig. 4. Flow is assumed to occur exclusively through the ends of the stream tube. The wind turbine is idealized as a uniform actuator disc, which induces a pressure discontinuity within the air stream passing through it. It is important to note that this analytical approach is general and not constrained to any specific type of wind turbine.

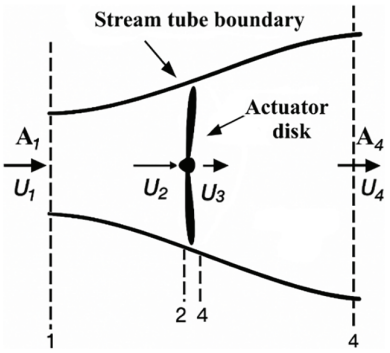

Figure 4: Actuator disc model of a wind turbine; U, mean air velocity; 1, 2, 3, and 4 indicate locations.

The Betz model, also known as actuator disk theory, operates under a set of idealized assumptions: the flow is considered homogeneous, incompressible, and steady; the rotor disk is modeled as having an infinite number of blades, effectively forming a continuous surface; the flow is inviscid, with no frictional or rotational losses; thrust is uniformly distributed across the rotor area; the wake downstream of the rotor is assumed to be non-rotating; and the static pressure far upstream and far downstream is equal to the ambient atmospheric pressure.

Consider an initial axial flow velocity U_1 approaching an actuator disc of area A, which exerts a constant axial thrust T. Let U_3 represent the axial velocity at the rotor plane, and U_4 the axial velocity in the far wake, where the air pressure has returned to the undisturbed ambient value such that $P_1 = P_4$. Let ρ denote the air density. In this one-dimensional model, the stream tube enclosing the rotor disc (as depicted in Fig. 4) has cross-sectional areas A_1 and A_4 far upstream and far downstream of the rotor, respectively. Applying the principle of conservation of mass under steady-state conditions and assuming a constant mass flow rate $\dot{m}$, the continuity equation across each cross-section leads to the following expression:

$$\dot{m} = \int \rho u dA = \rho U_1 A_1 = \rho U_{2,3} A = \rho U_1 A_4 \tag{1}$$

Applying Bernoulli's principle to the control volumes upstream and downstream of the rotor disk, respectively, where the flow of the upstream of the rotor is assumed inviscid, steady, and incompressible, and the downstream between the rotor plane and the far wake, where the pressure returns to ambient conditions. These applications provide the relationships between pressure and velocity in the stream tube, essential for deriving the thrust and power extracted by the actuator disc. Based on the principle of conservation of linear momentum for a control volume in a closed system, the net external force exerted on the fluid is equal in magnitude and opposite in direction to the thrust T acting on the wind turbine. For a one-dimensional, incompressible, and steady flow, the thrust can therefore be expressed as the rate of change of linear momentum across the stream tube:

$$T = U_1 (\rho AU)_1 - U_4 (\rho AU)_4 \tag{2}$$

Under the standard actuator-disc assumptions, namely that the static pressures far upstream and far downstream are equal and the axial velocity across the rotor disc is uniform, Eq. (2) simplifies directly to the classical thrust relation:

$$T = \frac{1}{2}\rho A_2 \left(U_1^2 - U_4^2\right) \tag{3}$$

To quantify the deceleration of the wind through the rotor, the axial induction factor a is introduced. It is defined as the fractional decrease in wind speed between the free stream and the rotor plane, such that $a = (U_1 - U_2)/U_1$. This formulation provides the basis for evaluating the power extracted by an ideal rotor. The turbine's performance is commonly characterized by the power coefficient $C_P = 4a(1-a)^2$. Thus, the mechanical power extracted from the free stream:

$$P = 1/2 C_p \rho A U^3 \tag{4}$$

Using the velocity relationships implied by the momentum theory and the actuator-disc model, the power coefficient can then be expressed directly in terms of the axial induction factor, leading to the well-known form of the wind turbine performance curve shown is Fig. 5. The power coefficient C_P is a unitless value that depends on the turbine design and represents the fraction of the available wind power that the turbine can capture. This theoretical Betz limit, indicates that no more than 59.26% of the kinetic energy in the wind can be extracted by an ideal wind turbine under steady, one-dimensional flow conditions. The same relationships can be substituted into the momentum expression to obtain the axial thrust on the rotor:

$$T = \frac{1}{2}\rho A U^2 C_T \tag{5}$$

where $C_T = 4a(1-a)$ is the thrust coefficient. The thrust coefficient reaches a theoretical maximum of 1.0 when $a = 1/2$, at which point the downstream velocity becomes zero. However, at the point of maximum power extraction ($a = 1/3$), the corresponding thrust coefficient is: $C_T = 8/9 \approx 0.888$.

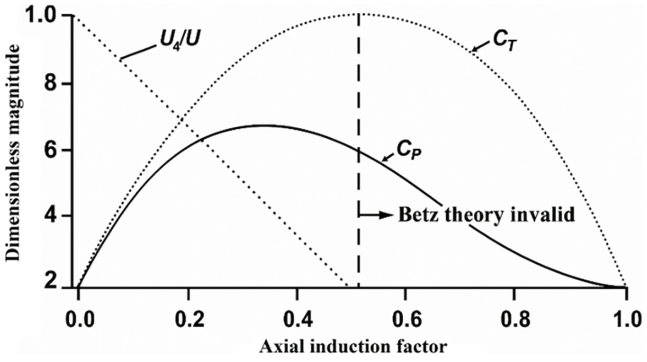

Figure 5: Variation of the power coefficient, thrust coefficient, and normalized downstream wind velocity as functions of the axial induction factor for an ideal Betz turbine.

Fig. 5 [6,19,20] presents the relationship between the power coefficient, thrust coefficient, and the normalized downstream wind velocity as functions of the axial induction factor for an idealized Betz turbine. The theoretical model is valid only up to an induction factor of 0.5. Beyond this limit, the assumptions of one-dimensional momentum theory break down, as the wake dynamics become increasingly complex. Flow separation, turbulence, and significant wake expansion occur when $a > 0.5$, phenomena that cannot be accurately described within the framework of the simple actuator disk approximation Wilson et al. [27].

2.2 Airfoils and General Concepts of Aerodynamics

Airfoils are the fundamental structural elements of wings, blades, and turbine rotors, designed to generate lift efficiently while minimizing drag. Their geometry defined by parameters such as chord length, camber, thickness, and leading and trailing edge profiles which directly influences aerodynamic performance, the terminology associated with airfoil features is summarized in Fig. 6 [20].

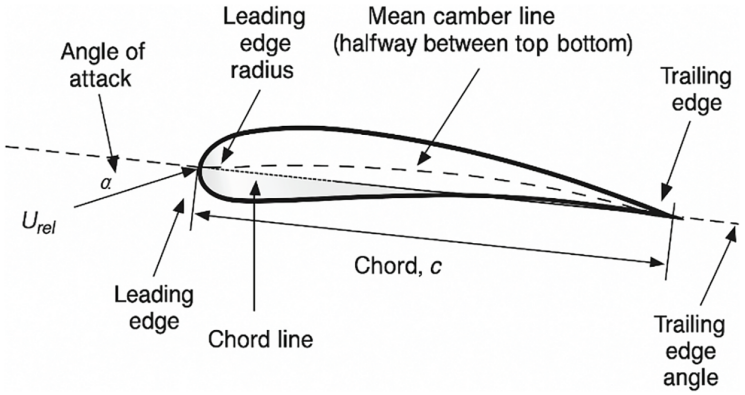

Figure 6: Principal terms employed to define airfoil geometry.

In aerodynamics, the forces acting on an airfoil arise from pressure differences created by the relative motion of air over its surfaces. When air flows faster over the curved upper surface than over the lower surface, a pressure differential develops, producing lift. At the same time, drag acts in the direction of the flow, composed of both viscous effects (skin friction) and pressure contributions (form drag). The performance of an airfoil is characterized by non-dimensional coefficients, primarily the lift coefficient C_L and the drag coefficient C_D,which depend on the angle of attack, Reynolds number, and Mach number.

When an airfoil is immersed in a free-stream of speed U_∞, two principal aerodynamic forces act on it: lift L, directed perpendicular to the free stream, and drag D, directed parallel to the free stream. By dimensional analysis, these forces can be written as

$$L = \frac{1}{2}\rho U_\infty^2 C_L A \tag{6}$$

$$D = \frac{1}{2}\rho U_\infty^2 C_D A \tag{7}$$

where ρ is the air density, A is the reference area (planform area), and C_L and C_D are the lift and drag coefficients, respectively. In wind turbine applications, the ratio C_L/C_D is a key indicator of aerodynamic efficiency. A higher ratio reflects greater lift generation relative to drag, which is particularly important in both wind turbine and aircraft design, as it enables maximum power extraction.

Fig. 7 illustrates the aerodynamic forces and moments acting on an airfoil section when immersed in a free-stream flow. The distribution of pressure over the airfoil surface, combined with viscous shear stresses, produces a resultant aerodynamic force that can be resolved into the lift and drag components. In addition, a pitching moment is generated due to the non-uniform distribution of these forces along the chord. By convention, these forces and the moment are referenced to the quarter-chord point ($c/4$ from the leading edge), which is a standard location in aerodynamics because it provides a nearly constant moment coefficient over a wide range of operating conditions. The directions of positive lift, drag, and moment are indicated

clarity in Fig. 7 [19,20]. Theory and experimental research have demonstrated that many fluid flow problems can be characterized using non-dimensional parameters, such as Reynolds numberR_e.

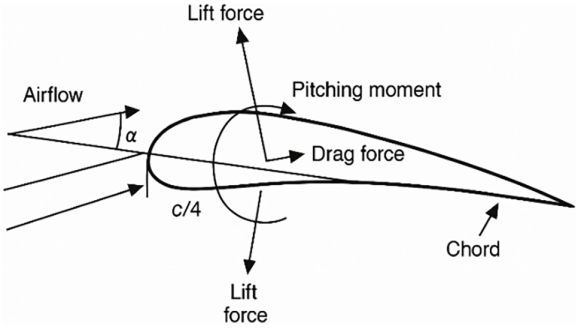

Figure 7: Forces and moments on an airfoil section. Positive directions for forces and moments are indicated by the arrow.

In addition to the Reynolds number, aerodynamic performance is described using non-dimensional force and moment coefficients, which are generally derived from wind tunnel experiments. For finite span (three-dimensional) airfoils, these coefficients are influenced by tip vortices and other spanwise effects. In contrast, two-dimensional data are obtained under conditions that eliminate end effects, often by testing with airfoil sections mounted between walls to simulate infinite span.

In wind turbine rotor design, two-dimensional airfoil data are commonly employed. These coefficients primarily lift C_L and drag C_D are tabulated across a range of angles of attack and Reynolds numbers, forming the foundation for predicting aerodynamic forces in blade element momentum theory and other rotor analysis methods. The two-dimensional lift coefficient, for instance, is defined as:

$$C_L = \frac{L'}{\frac{1}{2}\rho U^2 c} \tag{8}$$

where L' is the lift force per unit span and c is the chord length.

2.3 Flow Regimes of an Airfoil

The angle of attack α has a significant influence on airfoil performance. At relatively small values of α for about 7°–9° for the DU-93-W-210 airfoil and about 12°–14° for the FX63-137 airfoil [28–30], the airflow remains fully attached to the suction surface. In this regime, the lift coefficient C_L increases nearly linearly with angle of attack, while the drag coefficient C_D remains comparatively low. As α increases to approximately $7° \leq \alpha \geq 11°$ the airfoil enters a high-lift regime in which C_L reaches its maximum before beginning to decline. Stall occurs once the critical angle of attack is exceeded (typically between 11° and 16° depending on the Reynolds number). At this point, the boundary layer on the upper surface separates, producing a turbulent wake. This separation causes a sharp reduction in lift and a corresponding increase in drag. As illustrated in Fig. 8, the detachment of the boundary layer generates vortices in the wake, a defining feature of the stall regime.

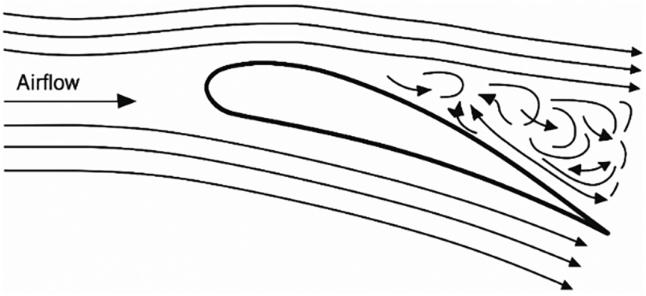

Figure 8: Airflow separation and vortex formation over an airfoil at stall.

In wind turbine applications, this partially stalled condition may arise at specific radial positions along the blade. Stall can also be deliberately employed in stall-regulated turbines with fixed-pitch blades, where the stalled region gradually progresses outward toward the blade tip as wind speed increases. This mechanism reduces aerodynamic efficiency and helps maintain nearly constant turbine power output above the rated wind speed. At very high angles of attack, extending up to 90°, the airfoil's behavior approaches that of a flat plate. At around 45°, lift and drag coefficients are approximately equal, whereas at 90° the lift vanishes ($C_L \approx 0$) and the drag reaches its maximum, dominated by pressure forces [19,20].

2.4 Structural Materials for Wind Turbine Blades

The structural integrity and reliability of wind turbine blades depend heavily on the materials used in their construction. Traditionally, blades have been manufactured using glass fiber–reinforced polymers (GFRPs) due to their favorable balance of low cost, moderate strength, and ease of processing. However, as turbine sizes have increased, the limitations of GFRPs such as reduced stiffness, lower fatigue resistance, and susceptibility to delamination and buckling have become more evident [6,20]. These constraints have encouraged a transition toward advanced materials that can meet the demands of larger and more durable blade systems.

Recent research has highlighted the potential of nanostructured reinforcements to significantly improve the performance of conventional composites. CNTs, in particular, have demonstrated exceptional tensile strength, stiffness, and thermal conductivity, with values far exceeding those of traditional fiber composites [31,32]. When embedded in polymer matrices, CNTs enhance stiffness, toughness, and crack resistance, thereby extending fatigue life and improving load transfer efficiency [33,34]. Despite these benefits, the widespread application of CNTs is constrained by high production costs and dispersion challenges, which are the subject of ongoing research [35–37]. Similarly, nano-silica has been widely investigated for its reinforcing capabilities. With high surface area and chemical stability, nano-silica can enhance compressive strength, stiffness, and durability of composite structures [38,39]. In the context of wind turbine blades, nano-silica improves stress distribution and fatigue resistance while also enhancing resistance to environmental degradation [40,41]. Challenges remain, however, in preventing nanoparticle agglomeration and ensuring safe handling in large-scale production environments [42].

To leverage the advantages of multiple nanomaterials, hybrid nanocomposites, such as CNT/nano-silica reinforced polymers, have been developed. These materials exhibit synergistic effects, combining the high stiffness and load-transfer capacity of CNTs with the toughness and chemical stability of nano-silica [43,44]. Hybrid nanocomposites provide an opportunity for tailoring properties to match specific blade requirements, such as enhanced fatigue resistance in high-stress regions or improved crack propagation resistance in trailing edges [45]. Although cost and processing complexities remain barriers, the development of structural

materials for wind turbine blades is moving beyond conventional GFRPs toward advanced nanomaterial-enhanced composites. CNTs, nano-silica, and hybrid nanocomposites represent a transformative step in blade engineering, offering superior fatigue performance, buckling resistance, and stress distribution while maintaining lightweight characteristics. This evolution in material strategies is critical to enabling the next generation of larger, more efficient, and longer-lasting wind turbines.

In this study, carbon nanotube (CNT)–based materials are modeled using an effective, homogenized elastic representation to investigate the potential structural benefits of stiffness-enhanced blade configurations. The CNT material considered here does not represent individual carbon nanotubes, nor does it correspond to a directly manufacturable bulk blade laminate. Instead, it represents an idealized CNT-reinforced polymer composite, intended to capture an upper-bound stiffness scenario under highly optimized assumptions of CNT dispersion, alignment, and load transfer.

An effective Young's modulus is adopted consistently throughout the analytical and numerical analyses. This value is selected based on upper-bound stiffness values reported in the literature for CNT-enhanced composite systems and is used here to explore the sensitivity of stress redistribution and global deformation behavior to increased material stiffness. The use of an isotropic effective modulus allows the influence of the internal structural configuration to be isolated without introducing additional complexity associated with detailed micromechanical modeling. The CNT-based material model should therefore be interpreted as a parametric representation rather than a direct material specification for blade manufacturing. The objective is not to predict absolute laminate performance, but to evaluate relative trends and potential structural advantages associated with novel internal architectures when higher stiffness materials are assumed. All comparative results are obtained using consistent material assumptions to ensure valid relative performance evaluation.

2.5 Campbell Theory in Wind Turbine Dynamics

Analyzing the dynamic response of wind turbine blades under rotational motion is a critical step in predicting and avoiding resonance conditions that may compromise blade performance and longevity. Campbell theory provides a foundational framework for analyzing the relationship between a rotating system's natural frequencies and its operational speed. The resulting Campbell diagram graphically represents how the natural frequencies of a blade vary with rotational speed, allowing designers to identify and avoid potential resonance conditions where vibrational modes and excitation harmonics coincide. In the process of wind turbine blade design, it is crucial to prevent the occurrence of resonant conditions, where a blade's natural frequency coincides with the rotor's rotational frequency or one of its harmonics corresponding to significant excitation loads [19]. Such resonances can lead to large-amplitude vibrations, increased noise, dynamic stresses, and accelerated fatigue damage. To identify and mitigate these conditions, designers commonly employ the Campbell diagram, a graphical representation that plots the blade's natural frequencies against the rotational speed of the turbine. From the origin of the plot, straight lines, known as harmonic rays, which represent integer multiples of the rotational frequency (e.g., $1x, 3x,$ *or* $6x$). Intersections between these harmonic lines and the natural frequency curves over the turbine's operational speed range indicate potential resonance zones. By ensuring adequate separation between excitation harmonics and natural frequencies, the Campbell diagram provides a valuable tool for optimizing blade geometry and material properties to achieve safe and stable dynamic performance [19].

In wind turbine systems, multiple sources of excitation, including aerodynamic forces, gravitational effects, and centrifugal loading, act periodically, producing harmonics directly related to the rotor speed. These harmonic excitations interact with the blade's natural vibration modes, typically classified as flapwise bending, edgewise bending, and torsional modes. As the rotor speed increases, a phenomenon known as

centrifugal stiffening occurs, causing a rise in the blade's natural frequencies and consequently shifting potential resonance points away from the operational range. This effect enhances the turbine's dynamic stability and contributes to reduced vibration amplitudes during operation.

Several researchers have applied Campbell-based analyses to better understand and predict wind turbine blade dynamics. Hansen [46] provided a comprehensive treatment of modal dynamics in isotropic rotor systems, demonstrating how Campbell diagrams can identify resonance and mode coupling in multi-bladed configurations. Xu et al. [47] investigated the influence of rotation on the natural frequencies of wind turbine blades, highlighting the impact of centrifugal stiffening on dynamic behavior. Hu et al. [48] employed strain-based operational modal analysis to detect resonances in a 5 MW horizontal-axis turbine using Campbell diagrams as diagnostic tools. More recent studies by Torres et al. [49] expanded the application of Campbell analysis to large-scale offshore turbines, emphasizing its effectiveness in detecting harmonic excitations, edgewise vibration phenomena, and dynamic amplification in flexible composite blades.

Collectively, these studies underscore the importance of Campbell theory as both a diagnostic and predictive method for dynamic stability evaluation in wind turbine design. It remains indispensable for verifying that operational speeds are safely separated from resonant conditions, guiding structural optimization, and validating numerical models. Within the scope of the present research, Campbell analysis is employed to ensure that the proposed diamond-lattice CNT-reinforced blade operates below critical resonance frequencies, demonstrating superior dynamic stability and vibration damping relative to conventional shear-web configurations.

3 Methodology

The advancement of wind energy technology is intrinsically tied to the continuous improvement of wind turbine blade design. As turbines grow in size to meet the global demand for renewable energy, their blades are increasingly subjected to complex aerodynamic loads, cyclic fatigue, and material degradation. Designing blades that can withstand these challenges while maintaining efficiency and cost-effectiveness requires not only innovative material solutions but also reliable tools for predicting structural and aerodynamic performance under realistic operating conditions. Computational modeling has therefore become a cornerstone in modern blade development, allowing engineers to evaluate new concepts before committing to large-scale manufacturing and testing [5]. Among the available modeling platforms, COMSOL Multiphysics® has emerged as a particularly powerful tool for this type of work. Known for its versatility in simulating coupled physical phenomena, COMSOL offers a unified environment where structural mechanics, aerodynamics, and material behavior can be studied in tandem. This capability is essential for wind turbine research, as blade performance depends not only on aerodynamic efficiency but also on structural stability and material resilience. By leveraging COMSOL's multiphysics framework, researchers can capture the interactions between airflow, composite materials, and internal reinforcements with a high degree of accuracy [50–52].

In this study, COMSOL Multiphysics was used to develop three models, for stress-strain, aerodynamics and materials-structure analysis, to evaluate the proposed improvements to conventional wind turbine blade designs. The software's pre-built physics interfaces for structural analysis, fluid flow, and composite mechanics allowed our team to model the blades under realistic conditions with fewer compatibility issues compared to running separate tools. Additionally, the flexibility to define custom geometries and materials was vital for testing advanced reinforcements, including nanomaterials and novel internal structural layouts. Parametric sweeps and optimization studies further enabled the systematic comparison of multiple design strategies, while finite element analysis (FEA) provided detailed insight into stress concentrations, deformation patterns, and fatigue behavior [53].

The blade modeled in this study was designed using dimensions representative of modern utility-scale wind turbines. Contemporary large wind turbine blades typically range from 80 to 130 m in length with maximum chord widths of approximately 4 to 8 m [54], and the geometry used in the simulations closely followed these values reported in the literature. Incorporating realistic blade dimensions ensures that the structural and dynamic responses captured in the analysis accurately reflect the behavior of full-scale turbine blades rather than simplified or idealized configurations [55,56]. To further approximate operational conditions, the applied loading was based on a realistic combined force distribution. The blade was subjected to an average uniformly distributed total load of 100–200 kN, in the stress strain model, representing the combined effects of aerodynamic wind pressure, along with the centrifugal forces generated during rotation and the gravitational loading acting on the blade mass. These forces act simultaneously on the structure during normal turbine operation, producing the complex loading environment replicated in the finite element analysis.

In the composite materials model, all structural simulations were performed using a simplified and reproducible loading framework for comparative analysis. Aerodynamic loading was obtained by converting the power expression in Eq. (4) into an equivalent steady three-dimensional pressure distribution derived from the total aerodynamic force and applied uniformly over the blade span and chord to generate global flapwise bending. Centrifugal loading was applied as a body force based on a prescribed constant rotor speed and the blade mass distribution, while gravity was included as a uniform body force acting in the vertical direction with the blade in a horizontal orientation. All load components were applied consistently to the full-scale blade models across all configurations to ensure valid and meaningful comparative results.

However, due to the significant computational cost associated with the development of large, high-fidelity finite element models, reduced-scale blade geometries were employed only during the preliminary model development stage. Specifically, models representing 0.1× and, in limited cases, 0.01× of the full blade size were used to facilitate geometry construction, mesh refinement, and solver verification while reducing memory usage and computation time. These scaled models were utilized solely to identify and resolve numerical issues and to optimize the meshing and boundary-condition implementation.

Once the numerical model was verified and stable behavior was achieved, all simulations used for data extraction, comparison, and discussion were performed using the full-scale blade geometry with consistent material properties, loading conditions, and boundary constraints. Consequently, the results reported in this study are not influenced by geometric or load scaling effects, and no similarity assumptions are required for the interpretation of the presented stress, strain, or displacement results.

In addition to geometric scaling, the mesh resolution was tailored to the structural importance of each domain and refined iteratively to balance accuracy and computational time. High-resolution second-order tetrahedral elements were applied in regions with high stress gradients such as the blade root, leading and trailing edges, and internal lattice intersections, while mapped meshes were used in low-sensitivity areas and during preliminary simulations. A mesh convergence study was conducted by progressively refining the mesh until changes in peak von Mises stress, deformation, and natural frequencies fell within 1%–3%, confirming numerical stability. Final models contained approximately $0.1 - 1.0 \times 10^6$ elements, ensuring accurate representation of both global structural behavior and localized stress responses.

Despite these scaling and meshing adjustments, the use of proportionally accurate blade dimensions and realistic combined loading remains essential because blade size, centrifugal stiffening, gravitational effects, and aerodynamic pressure directly influence bending moments, stress distribution, and natural frequencies. The scaled models therefore continue to capture the dominant structural and dynamic behaviors of full-scale blades, ensuring that the comparative results remain valid, reliable, and applicable to next-generation wind turbine blade designs.

Although COMSOL Multiphysics® provides a powerful platform for evaluating the structural and dynamic behavior of wind turbine blades, several limitations must be acknowledged. The finite element analysis relies on idealized assumptions such as linear material behavior, perfect geometry, and simplified boundary conditions, which do not fully capture nonlinear deformation, manufacturing imperfections, or progressive damage mechanisms present in real blades.

Aerodynamic loads were represented in a simplified manner and not fully coupled through fluid–structure interaction, potentially affecting the accuracy of predicted excitation forces and dynamic responses. Additionally, rotational effects such as turbulence-induced fluctuations, transient aerodynamic disturbances, and operational variability are not fully represented within the modeling environment. Complementing the structural analysis, the CFD simulations also involve inherent limitations that influence accuracy. While the mesh resolution was sufficient for capturing global flow patterns, it may not fully resolve fine-scale turbulence structures or localized pressure gradients near the blade surface. The turbulence model employed provides an approximation of atmospheric flow and cannot accurately reproduce transient eddies, dynamic stall, or complex separation behavior encountered in variable wind conditions. Furthermore, boundary conditions were simplified by assuming uniform inlet flow and steady operating states, omitting the influence of realistic environmental factors such as turbulence intensity, wind shear, and yaw misalignment.

Finally, with respect to material-related limitations, the CNT-based material is represented using an isotropic effective elastic modulus and does not explicitly account for laminate orthotropy, CNT volume fraction, dispersion quality, or manufacturing constraints. Accordingly, this material representation should be interpreted as an idealized upper-bound model rather than a directly deployable blade laminate. In addition, the layered structural representation adopted in this study is a numerical abstraction intended to capture global stiffness effects and does not reflect detailed industrial spar cap or shell layup architectures. The present analysis is further limited to static structural response, and dynamic, fatigue, and aeroelastic effects are not considered.

3.1 Model Validation

3.1.1 Structural Mechanic Model

To establish confidence in the structural modeling framework prior to its application to the full blade configuration, a verification study was conducted using an idealized cantilever beam. For verification purposes, an idealized hollow rectangular cantilever beam was modeled with an overall root width of 8 m, a thickness of 4 m, and a total length of 80 m. The beam incorporates external walls and internal stiffening two webs, each with a uniform thickness of 0.5 m, forming a multi-cell box-type cross-section representative of the structural layout typically found near the wind turbine blade root. The beam was modeled as a carbon nanotube (CNT) composite material and assumed to exhibit linear elastic behavior. CNT composites typically have an effective Young's modulus in the range of 1000–1300 GPa [57]; in this study, a value of 1000 GPa was adopted. A uniformly distributed load of 200 kN was applied along the entire span to replicate the global bending response under aerodynamic loading. This simplified configuration provides a controlled benchmark in which analytical solutions can be directly compared against numerical results, ensuring the correctness of the finite element formulation, boundary conditions, and material definitions.

Analytical bending stresses and strains were obtained using Euler–Bernoulli beam theory for a cantilever subjected to a uniformly distributed load. The distributed loading generated a maximum bending moment of 8×10^6 N/m at the fixed root. Based on hand calculations implemented in Matlab®, the maximum bending stress at the root section is predicted to be approximately 0.56603 MPa. Since bending stress is

governed solely by the applied load and the cross-sectional geometry, this value is independent of the assumed carbon nanotube (CNT) elastic modulus.

The corresponding elastic strain depends on the selected material stiffness and remains within the expected range for CNT-based composites under the applied loading. Using the same Matlab® implementation, the volumetric elastic strain at the blade root is calculated to be 5.66038×10^{-7}. A complete derivation of the analytical formulation and the associated Matlab® code for the simplified cantilever beam are provided in Appendix A.

To validate the analytical solution, a three-dimensional finite element model was developed in COMSOL Multiphysics using identical geometry, material properties, boundary conditions, and loading. The resulting von Mises stress distribution is shown in Fig. 9a. As observed in the figure, the maximum stress is concentrated near the fixed root of the beam, where the bending moment is highest, and gradually decreases toward the free end. The peak stress predicted by COMSOL for the simplified beam model is approximately 5.3864×10^5 Pa, compared with 5.66038×10^5 Pa obtained from the Matlab® calculations, corresponding to a relative difference of 5.57%. This close agreement confirms the accuracy of the numerical stress prediction.

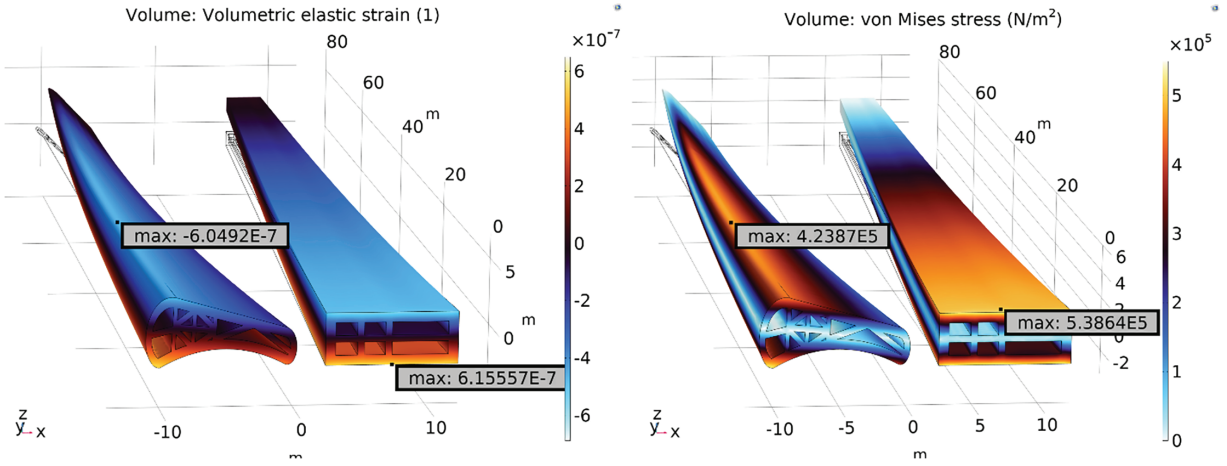

Figure 9: Structural model validation results for the simplified cantilever beam: (**a**) von Mises stress distribution for the simplified hollow box-beam model, and (**b**) Volumetric elastic strain showing a consistent spatial trend. The close agreement between the analytical predictions and the COMSOL results confirms the accuracy of the numerical implementation.

Fig. 9b presents the volumetric elastic strain distribution along the beam. The maximum strain predicted by COMSOL is 6.15557×10^{-7}, while the analytical Matlab® solution yields a value of 5.66038×10^{-7}, resulting in a relative difference of approximately 8.04%. The strain contours in both approaches exhibit the same spatial trend, with peak values occurring near the fixed root and decreasing smoothly along the span toward the free end. This behavior is fully consistent with classical cantilever beam theory and the associated bending stress distribution.

The strong agreement in both magnitude and spatial distribution of von Mises stress and volumetric elastic strain between the analytical Matlab® calculations and the COMSOL simulations demonstrates that the numerical model accurately captures the global bending response of the hollow, stiffened cantilever structure. This validation provides confidence in the finite element implementation and supports its use for subsequent analyses involving the full blade geometry and more complex internal structural configurations.

3.1.2 Composite Materials Model

To further validate the numerical implementation of the composite blade model, the built-in COMSOL *wind_turbine_composite_blade* benchmark [56], was first reproduced to establish a reference solution. The benchmark results for static tip displacement, stress distribution, and natural frequencies were successfully replicated, confirming the correctness of the baseline geometry, boundary conditions, loading definitions, and solver settings. Subsequently, the original composite material properties were replaced with the proposed carbon nanotube (CNT) orthotropic material model while maintaining identical geometry, loading, constraints, mesh, and study configurations. Quantitative validation was performed by comparing the maximum von Mises stress using the relative difference expression.

$$R_{diff} = \left[\frac{|\sigma_{bench} - \sigma_{CNT}|}{\sigma_{bench}} \right] \times 100 \tag{9}$$

where $\sigma_{bench} = 396.283$ MPa is the benchmark peak stress and $\sigma_{CNT} = 372.937$ MPa is the corresponding value obtained from the CNT-enhanced model, yielding a stress reduction of approximately 5.89%.

Displacement-based validation was carried out by comparing the global deformation response at key locations along the blade. The benchmark model predicted a maximum tip displacement magnitude of 2.259 m and a displacement of 0.44317 m at the last evaluation point along the span, whereas the CNT-based model yielded corresponding values of 0.9837 and 0.0643 m, respectively. The significant reduction in displacement magnitudes is consistent with the increased stiffness introduced by the CNT-reinforced composite material. In addition, modal analysis showed an upward shift in the natural frequencies, further confirming the expected stiffness-driven dynamic behavior.

Consequently, the close agreement in stress levels and the physically consistent reductions in displacement and strain, together with increased modal frequencies, confirm the correct implementation of the CNT orthotropic material properties and laminate orientation. This benchmarking exercise provides strong confidence in the reliability of the numerical framework and supports the validity of the predicted performance improvements for the proposed CNT-reinforced wind turbine blade.

Additionally, the blade geometry and material configuration from the COMSOL *wind turbine composite blade* benchmark model were imported into the developed numerical framework and subjected to the same boundary conditions and loading scenarios as the proposed blade.

The resulting stress distributions are presented in Fig. 10, which compares the von Mises stress contours of the proposed CNT-reinforced blade with those obtained from the imported benchmark blade. The close correspondence between the two stress fields demonstrates that the developed model reliably reproduces the expected structural response. This agreement confirms that the numerical framework is capable of producing scientifically credible results and can be confidently employed for further analysis of the proposed blade design.

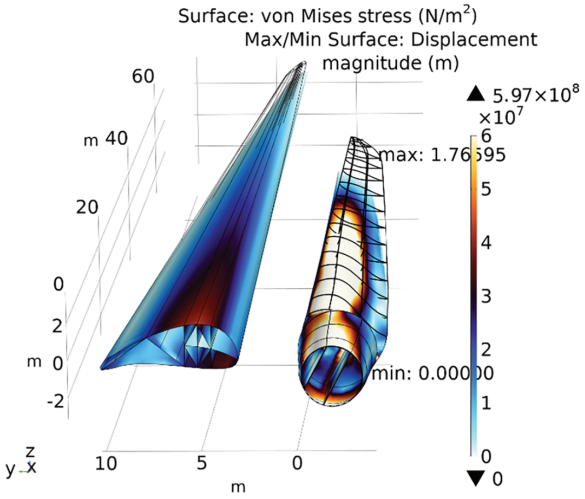

Figure 10: Von Mises stress comparison between the proposed CNT-reinforced blade and the imported benchmark blade under identical loading and boundary conditions.

3.2 Evolution of Internal Blade Structures

Despite incremental refinements, the basic conventional wind turbine blade structure, shown in Fig. 11a, continues to experience stress concentrations at the root, spar caps, and leading and trailing edges. These localized weaknesses often result in crack initiation, accelerated fatigue, and in some cases, catastrophic structural failure. Such shortcomings highlight the need for innovative reinforcement strategies capable of improving stress distribution, buckling resistance, and overall structural reliability. The first redesign concept, illustrated in Fig. 11b, introduced basic longitudinal stiffeners within the hollow cross-section. These elements increased stiffness along the chord but did not adequately address localized stress buildup near the root and trailing edge. Although this modification provided modest improvements in load distribution, the risk of premature fatigue persisted. A second iteration presented in Fig. 11c, incorporated additional parallel stiffeners and diagonal supports. This layout was more effective in channeling aerodynamic and gravitational loads along the blade span, thereby enhancing torsional rigidity.

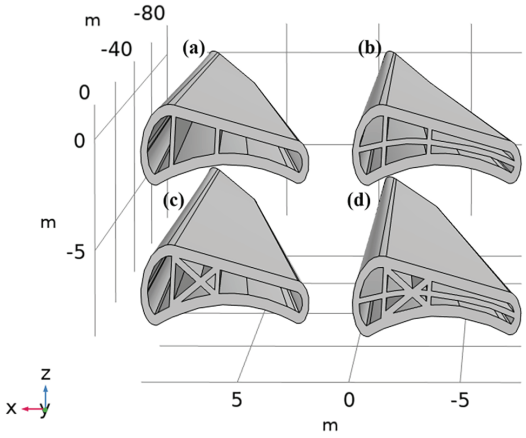

Figure 11: Evolution of internal reinforcement concepts for wind turbine blades modeled in COMSOL Multiphysics: (**a**) conventional blade with basic spar webs, (**b**) blade with additional longitudinal stiffeners, (**c**) blade with cross-bracing reinforcement, and (**d**) blade with advanced lattice-style diamond reinforcements.

However, the added material increased blade mass and manufacturing complexity, while buckling resistance under extreme loading remained insufficient. To improve upon earlier concepts, a third model given in Fig. 11d, introduced cross-bracing within the spar web. This X-shaped reinforcement provided better load transfer and significantly reduced deformation under bending. Nevertheless, stress concentrations at intersecting joints created new potential failure points, limiting the long-term fatigue benefits.

Fig. 11 summarizes the iterative development of wind turbine blade internal structures, progressing from conventional layouts to advanced reinforcement strategies. These cross-sections highlight how successive design modifications aimed to improve stress distribution, buckling resistance, and vibration control, with the final configuration (d) used as the reference baseline for evaluating the new blade concept proposed in this study.

3.3 Evolution of Proposed Internal Designs

In this study, a series of novel internal reinforcement layouts were systematically developed and tested to identify an optimal wind turbine blade internal structure. Each iteration sought to overcome the shortcomings observed in conventional blade architectures, particularly stress concentration at the root, buckling near the spar caps, and deformation along the trailing edge. The progressive development of these concepts illustrates an evolutionary pathway, where lessons learned from each configuration directly informed the next. The first proposed design introduced simplified longitudinal and diagonal stiffeners integrated within the airfoil profile. This initial attempt improved structural stiffness compared to the conventional hollow blade, distributing stresses more evenly across the chord. However, localized stresses near the root and trailing edge remained, indicating the need for a more interconnected reinforcement framework. A second design iteration expanded upon this by introducing the first diamond diagonal members to connect spar caps and webs. This enhanced load transfer efficiency and provided greater torsional rigidity, reducing deformation under aerodynamic loading. Despite these gains, the design introduced weight penalties and did not fully address fatigue issues at stress-critical regions, particularly around joint intersections. To further advance the concept, a third configuration incorporated cross-bracing in the form of diamond-shaped with a vertical spar reinforcements within the spar region. This lattice-like arrangement provided improved connectivity between internal members, effectively redistributing loads and enhancing resistance to buckling. Additionally, vibration damping improved, reducing susceptibility to resonance-induced fatigue. However, this layout still demonstrated inefficiencies in material use, with overlapping reinforcements adding unnecessary weight. The final proposed design incorporated insights from all previous iterations into a refined diamond-patterned lattice structure strategically distributed along the internal span of the blade. This optimized configuration integrates longitudinal, diagonal, and cross-bracing elements into a unified diamond geometry, forming a highly efficient internal load-carrying framework. The arrangement enhances bending and torsional stiffness, minimizes shear deformation, and promotes a uniform stress distribution under combined aerodynamic and centrifugal loads.

Finite element simulations confirmed that this diamond-reinforced configuration effectively reduced peak von Mises stress and strain concentrations at critical regions such as the blade root and leading edge, while maintaining a low overall structural mass. The resulting design achieved an optimal balance between stiffness, strength, and material efficiency, translating into improved fatigue life, buckling resistance, and dynamic stability during turbine operation. Beyond its structural advantages, the diamond lattice also provided measurable vibration damping and noise reduction, attributed to its ability to mitigate resonance-induced vibration modes. The lattice ensured smoother load transfer between the spar caps and the

aerodynamic shell, thereby enhancing structural longevity and aerodynamic performance. This configuration represents the culmination of an iterative development process, integrating geometric optimization and material refinement to achieve a lightweight yet robust structural solution.

Fig. 12 illustrates the systematic refinement process that culminated in the optimal reinforcement architecture adopted in this study. The figure shows the evolution of the proposed internal reinforcement concepts for the wind turbine blade, modeled in COMSOL Multiphysics. (a) The initial configuration introduces simple longitudinal and diagonal stiffeners, which improve global stiffness but leave notable stress concentrations near the root and trailing edge. (b) The second design incorporates the first diamond-shaped diagonal members, enhancing load transfer and torsional rigidity, though added weight and localized fatigue concerns remain. (c) A more interconnected lattice is introduced through expanded cross-bracing and a central vertical spar, improving buckling resistance, load redistribution, and vibration damping, yet still exhibiting inefficiencies in material usage. (d) The final optimized design integrates longitudinal, diagonal, and cross-bracing elements into a unified diamond-patterned lattice, forming a highly efficient internal load-carrying framework that minimizes deformation, reduces stress concentrations, and enhances stiffness under combined aerodynamic and centrifugal loads.

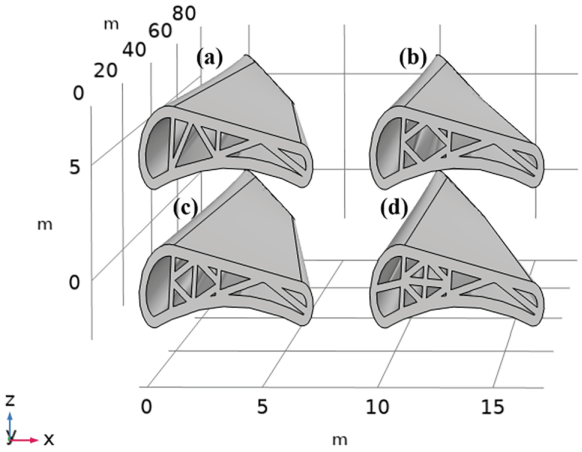

Figure 12: Evolution of internal blade reinforcement designs: (**a**) longitudinal stiffeners, (**b**) diamond-diagonals, (**c**) expanded cross-bracing, and (**d**) final optimized diamond lattice.

3.4 Proposed Internal Design Analysis

The proposed internal design introduces a novel diamond-lattice reinforcement structure aimed at enhancing the mechanical performance, fatigue resistance, and overall stability of modern wind turbine blades. This configuration replaces the conventional X-shaped reinforcement design with an interconnected network of diagonal and longitudinal members that form a unified load-carrying framework. The diamond-shaped lattice redistributes stresses more evenly throughout the blade span, reduces local stress concentrations at critical zones such as the root and spar caps, and increases global stiffness without significantly increasing overall weight. This geometric arrangement allows for superior load transfer efficiency and improved energy absorption capacity, particularly under combined aerodynamic, centrifugal, and gravitational loads.

To evaluate the structural performance of the proposed configuration, detailed finite element simulations were conducted using COMSOL Multiphysics®. The analyses included static and fatigue load cases under realistic operating conditions. The results demonstrate that the diamond-lattice blade achieved a notable reduction in peak von Mises stress and a more uniform stress distribution compared to the

conventional X-shaped blade. The improved stress uniformity results in a 11%–16% reduction in peak stress and a corresponding increase in fatigue life per design iteration, accompanied by enhanced resistance to buckling and reduced out-of-plane deformation. These findings confirm that the lattice configuration not only improves mechanical strength but also contributes to longer operational life and reduced maintenance requirements, aligning with the goals of next-generation renewable energy systems.

In addition to structural geometry optimization, the proposed design incorporates advanced nanocomposite materials, particularly CNT, nano-silica, and hybrid nanocomposite reinforcements, within the blade's composite matrix. CNT-reinforced laminates were found to provide the most favorable balance between stiffness, weight, and damping capacity. Their exceptional strength-to-weight ratio and ability to improve interlaminar bonding result in increased stiffness, reduced vibration amplitudes, and greater resistance to crack propagation under cyclic loading. The combination of an optimized internal structure and nano-enhanced materials thus represents a hybrid engineering approach that bridges structural and material design, achieving superior static and dynamic performance while preserving manufacturability.

3.5 Dynamic Analysis Based on Campbell Theory

A critical part of validating the proposed blade's performance involves analyzing its dynamic behavior using Campbell theory, which provides essential insight into vibration characteristics and resonance tendencies in rotating systems. The Campbell diagram graphically depicts the relationship between the blade's natural frequencies and its rotational speed, enabling identification of potential resonance conditions where excitation frequencies coincide with structural natural frequencies. These excitations arise from periodic aerodynamic and inertial forces acting on the rotating blades and are harmonically related to the rotor speed. Each harmonic corresponds to a distinct number of excitations per revolution, forming a set of excitation lines on the diagram.

In the Campbell diagram of the proposed CNT-reinforced wind turbine blade, each curve represents a distinct vibration mode, such as flapwise bending, edgewise bending, or torsional response, while the diagonal lines correspond to harmonic excitation frequencies. Intersections between these sets of curves signify potential resonance conditions, which can cause large vibration amplitudes and lead to structural failure if they occur within the operational speed range. However, for the proposed blade design, no intersections were observed between the excitation lines and the natural frequency curves within the normal operating regime. This indicates that the blade operates safely below its critical resonance speeds and possesses excellent dynamic stability.

As the rotational speed increases, the natural frequencies exhibit a slight upward trend which a result of centrifugal stiffening, where rotation increases the apparent stiffness of the blade. This beneficial effect contributes to widening the separation between frequency modes, thereby minimizing the risk of resonance and modal coupling. The CNT-reinforced composite material further enhances damping properties, reducing the amplitude of vibrational response and improving the blade's resilience under continuous rotational loading. Thus, the blade exhibits smoother dynamic performance, lower vibration amplitudes, and extended fatigue life, confirming that the integration of the diamond-lattice structure and CNT-based materials significantly improves overall stability and operational safety.

Consequently, the proposed internal design analysis demonstrates that combining geometric optimization with nanomaterial enhancement offers a transformative pathway for the design of wind turbine blades. The proposed diamond-lattice configuration not only mitigates high-stress regions but also enhances stiffness, dynamic stability, and fatigue resistance. Supported by Campbell analysis and finite element validation, this integrated approach establishes a foundation for developing lighter, stronger, and longer-lasting blades that can significantly advance the reliability and efficiency of future wind energy systems.

4 Results and Discussion

The results of this study provide a comparative evaluation of conventional wind turbine blade structures and newly proposed reinforcement configurations developed through COMSOL Multiphysics modeling. As turbine blades continue to increase in size, structural demands grow more complex, with failures frequently originating from stress concentrations at the root, spar caps, and leading and trailing edges. These weaknesses in conventional hollow designs often lead to fatigue, buckling, and deformation under prolonged aerodynamic, centrifugal, and gravitational loading. To address these limitations, the proposed design introduces a systematic evolution of internal reinforcement strategies aimed at improving load redistribution, stiffness, and fatigue resistance while maintaining weight efficiency.

The numerical simulations enabled a detailed assessment of how each evolutionary step in the design process influenced stress distribution, buckling resistance, deformation behavior, and vibration control. Conventional blade models were first examined to establish baseline performance metrics, clearly highlighting their susceptibility to localized stress concentrations and reduced fatigue life. Successive iterations incorporating longitudinal stiffeners, diagonal supports, and cross-bracing progressively improved structural performance; however, these designs often involved trade-offs, such as increased mass or inefficient material utilization. The diamond-lattice configuration emerged as the optimal solution, achieving a favorable balance between stiffness and weight efficiency while significantly reducing stress concentrations and enhancing fatigue resistance.

Although the diamond-lattice internal structure represents a more complex geometry than traditional shear-web configurations, recent advances in digital design and manufacturing technologies substantially enhance its practical feasibility. Modern computer-aided design and manufacturing tools allow precise generation and optimization of complex lattice geometries, ensuring compatibility with established blade design workflows. In particular, additive manufacturing and large-scale composite 3D printing technologies enable the fabrication of intricate internal lattice structures with high geometric accuracy and reduced tooling requirements. Furthermore, established composite manufacturing techniques such as filament winding, automated fiber placement, and pultrusion can be adapted to produce prefabricated lattice subcomponents, which can be integrated into the blade shell during layup and bonding processes. Hybrid manufacturing approaches that combine additively manufactured internal cores with conventional composite shells further improve scalability and cost-effectiveness for utility-scale wind turbine blades.

Consequently, the proposed diamond-lattice design not only demonstrates superior structural performance in terms of stress reduction, fatigue life, and buckling resistance, but also aligns well with emerging and established manufacturing technologies. This compatibility reinforces the practical applicability of the proposed reinforcement concept and supports its potential implementation in next-generation wind turbine blade designs.

4.1 Stress Distribution

Finite element analysis revealed a clear improvement in structural performance for the proposed diamond-lattice reinforced blade compared to the conventional market design. To quantify this improvement, the percentage reduction in maximum stress, strain and fatigue was calculated using the relative difference expression given in Eq. (9).

As shown in Fig. 13, both stress values were extracted directly from the simulation outputs. Using Eq. (9), the percentage improvement was then calculated, providing a consistent and transparent basis for comparing the two structural configurations. This metric clearly highlights the reductions in stress achieved through the

incorporation of the diamond-lattice reinforcement, confirming the structural advantages of the proposed blade architecture.

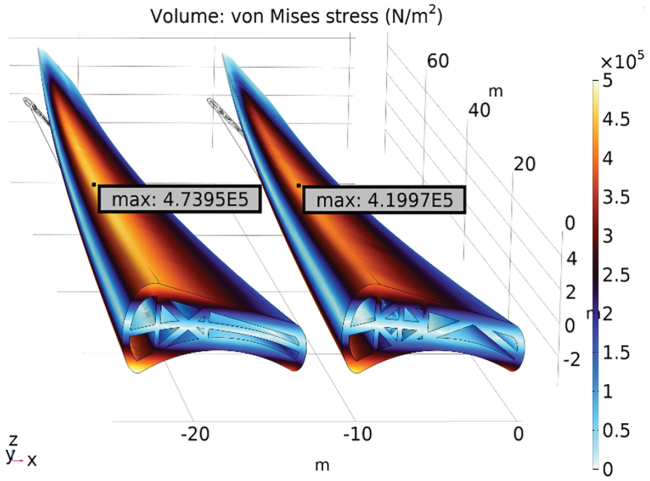

Figure 13: The Von Mises stress plots demonstrate that the redesigned blade experiences approximately 11.38% lower overall stress compared to the conventional blade.

Fig. 13, illustrates the Von Mises stress contours show that the conventional blade exhibits elevated stress concentrations near the root and along the trailing edge, both of which are critical zones for crack initiation and delamination.

In contrast, the proposed blade demonstrates a reduction of 11.38% in overall stress intensity, with stresses redistributed more uniformly along the blade surface. This improved stress distribution reduces the likelihood of localized material failure and supports longer operational lifetimes.

Three-dimensional stress distribution visualization and strain distribution maps further confirm these findings. The diamond-lattice geometry facilitates smoother load transfer between spar caps and the aerodynamic shell, enhancing global stiffness and reducing torsional and flapwise deformations. These improvements are particularly important for large-scale turbines, where excessive deformation and cyclic fatigue can accelerate structural degradation. Quantitatively, the stress reduction translates into a projected 11.38% and enhancement in buckling resistance, providing a significant safety margin under high-load, long-duration operating conditions. Overall, the proposed configuration promotes superior stress distribution, increased stiffness, and improved structural resilience, demonstrating its suitability for next-generation wind turbine applications.

4.2 Fatigue Analysis

Fatigue behavior was evaluated using the Dang Van and Findley multiaxial fatigue criteria available in COMSOL Multiphysics. These critical-plane models assess fatigue damage based on combined normal and shear stress components and are widely applied in engineering fatigue analyses. The fatigue evaluation was performed using stress results obtained from representative static loading conditions, providing a comparative measure of fatigue susceptibility across different blade configurations. Traditional S–N curve–based approaches and cumulative damage models such as Miner's rule were not employed in this study because the objective was not to predict absolute fatigue life under detailed load spectra, but rather to perform a comparative assessment of fatigue sensitivity using multiaxial stress-based criteria that are more suitable for evaluating complex three-dimensional stress states within the proposed structural configurations.

Buckling behavior was assessed using linear eigenvalue buckling analysis to estimate the critical load factors and identify potential instability modes. This approach provides an efficient and consistent metric for comparing buckling resistance among configurations. Nonlinear geometric effects and post-buckling response were not considered in the present study. This combined fatigue and buckling assessment framework is sufficient for the intended comparative evaluation of structural concepts and is consistent with established modeling practices documented in COMSOL Multiphysics.

The fatigue performance of the two blade designs was evaluated using the fatigue usage factor contours presented in Fig. 14. The conventional blade demonstrates elevated fatigue usage along the suction side of the shell and at the trailing edge, which are regions highly susceptible to crack initiation under cyclic aerodynamic loading.

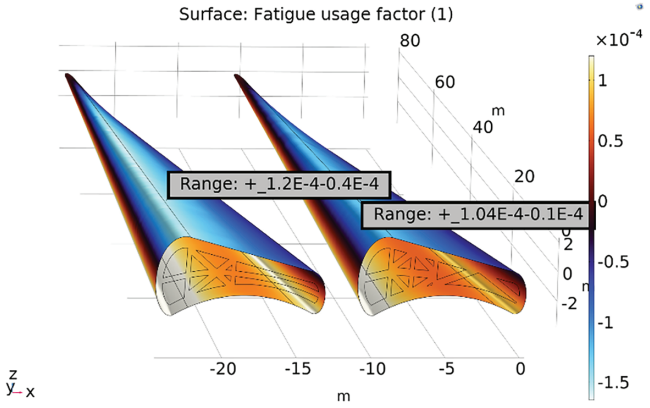

Figure 14: Fatigue usage factor comparison between conventional and proposed blades, showing reduced fatigue hotspots and improved fatigue life in the optimized diamond-lattice design.

These localized fatigue hotspots correspond with the stress concentrations identified in the Von Mises analysis, reinforcing the well-documented structural vulnerabilities of current market blades. In contrast, the proposed blade equipped with the diamond-lattice reinforcement exhibits a far more favorable distribution of fatigue usage factors. The reduction of fatigue intensity across the majority of the span indicates that the optimized internal geometry not only redistributes stresses but also alleviates cyclic strain accumulation, thereby slowing the initiation and propagation of cracks.

The percentage improvement calculated using Eq. (9) corresponds to a 14.38% increase in fatigue life, significantly reducing the risk of premature blade failure during long-term turbine operation.

The more uniform fatigue usage also enhances structural reliability by minimizing the potential for delamination and localized damage, which are common failure modes in composite blades. Collectively, these results confirm that the proposed design achieves superior fatigue resistance, aligning with the stress reduction findings and supporting its viability for deployment in high-load, long-duration wind energy applications.

4.3 Strain Analysis and Structural Implications

Strain analyses provide deeper insight into the deformation behavior of the blades, complementing the stress and fatigue findings. The volumetric elastic strain results, presented in Fig. 15, highlight a different but equally important aspect: how the blade responds to volumetric changes associated with tensile and compressive loading.

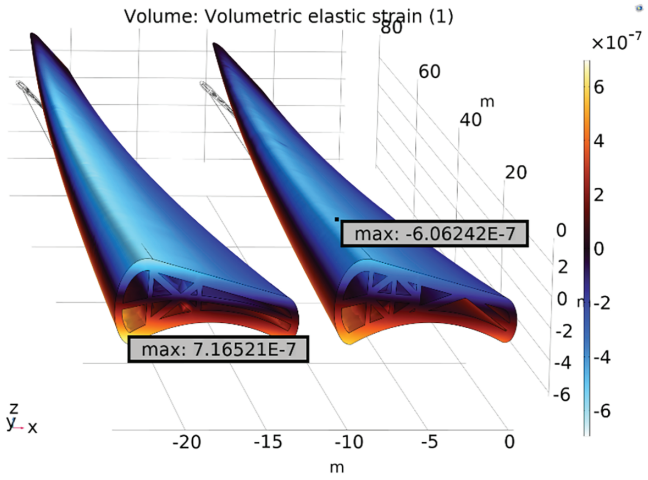

Figure 15: Comparison of volumetric elastic strain for conventional and proposed blades, illustrating lower and more evenly distributed volumetric strain in the optimized blade, reducing the risk of delamination and localized material separation.

The conventional blade exhibits pronounced strain peaks near the trailing edge and root, with values exceeding those of the proposed blade by more than 1.102. In contrast, the proposed design shows an approximate 15.39% reduction in strain, mitigating the localized expansion and contraction that can initiate delamination in composite layers.

In the proposed blade, however, the diamond reinforcement ensures that volumetric strains remain lower and more evenly distributed across the shell and spar regions. This improved balance reduces the risk of material separation under fluctuating aerodynamic loads, a common failure mode in large composite structures. The second invariant of the deviatoric elastic strain tensor, shown in Fig. 16, reveals how shear-related distortions are distributed along the blade.

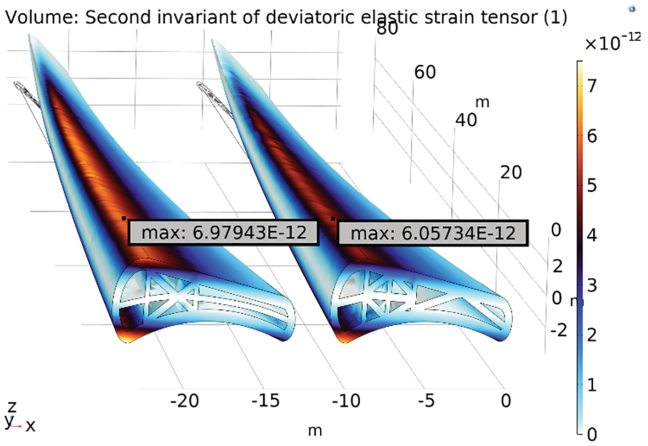

Figure 16: Comparison of the second invariant of deviatoric elastic strain for conventional and proposed blades, showing reduced shear strain concentrations and more uniform strain distribution in the optimized diamond-lattice design.

In the conventional blade, these strains are concentrated toward the mid-span and root, with values approaching 6.979×10^{-12}, indicating regions of high localized distortion that can accelerate micro-crack

initiation and progressive material damage. Both complementary measures, deviatoric strain capturing shear-driven deformation and volumetric strain quantifying dilation and compression, provide a comprehensive understanding of blade behavior under load.

The results confirm that the diamond-lattice internal architecture not only reduces overall strain magnitudes but also mitigates both shear and volumetric strain concentrations.

This dual improvement enhances structural reliability, delays the onset of fatigue damage, and provides greater resistance against buckling and delamination.

Collectively, the proposed design achieves a 13.21% more robust balance of stiffness and flexibility, contributing to longer service life, reduced maintenance costs, and higher operational reliability in industrial wind turbine applications.

In practical wind turbine operation, the observed improvements in strain behavior directly address some of the most common and costly blade failure modes. Trailing-edge cracks and delamination are often initiated by excessive volumetric strain peaks in conventional designs, particularly under fluctuating aerodynamic loads. By reducing these peaks and distributing volumetric strain more uniformly, the proposed diamond-lattice blade significantly lowers the likelihood of such failures. Similarly, root buckling and shear-driven material damage, typically associated with concentrated deviatoric strains, are mitigated by the smoother distribution and reduced magnitudes observed in the optimized design. These findings suggest that the proposed blade architecture not only enhances theoretical performance metrics but also directly improves operational reliability, reducing downtime, inspection frequency, and replacement costs. In the context of large-scale wind farms, where blade failures contribute substantially to levelized cost of energy, the adoption of this reinforced architecture has the potential to deliver both economic and engineering benefits by extending blade service life and improving structural safety under demanding operating conditions.

4.4 Aerodynamic Performance and Flow Analysis

To complement the structural evaluations, a detailed aerodynamic analysis was conducted using COMSOL Multiphysics. The blade section employed in this study was designed with an airfoil profile closely resembling the DU 93-W-210 and FX63-137 are widely used thick airfoil optimized for wind turbine applications. These choices were deliberate, as the known for their favorable lift-to-drag characteristics and structural thickness, making it suitable for large rotor blades. To better replicate realistic operating conditions, the modeled blade was also twisted longitudinally by an angle of 20° along its span, mimicking the aerodynamic tailoring commonly employed in commercial wind turbine blades to maintain favorable angles of attack across different radial positions [28]. With the use of this airfoil geometry and a twisted blade model, the aerodynamic simulations were developed to capture both local flow characteristics and overall blade performance across a range of angles of attack. This configuration provides a representative basis for evaluating lift and drag generation, as well as flow separation phenomena, ensuring that the results can be meaningfully compared with both theory and experimental data reported in the literature. As noted previously, the typical operating angle of attack for a DU 93-W-210 airfoil lies between 7° and 9° while for FX63-137 airfoil lies between 12° and 14° [30]. In this study, the aerodynamic analysis was initiated at 0° and was then incrementally increased in successive steps until the simulation either failed to converge or produced unrealistic results, thereby identifying the practical limits of the model in capturing post-stall aerodynamic behavior The inability of the model to provide reliable solutions beyond this range aligns with well-established aerodynamic theory and published findings, which document stall onset and rapid performance degradation at similar angles for comparable airfoil profiles [29,58,59].

Fig. 17 illustrates the velocity field and streamline evolution at different angles of attack. At 0° (a), the airflow remains attached, with smooth and continuous streamlines wrapping around the blade and no evidence of vortex formation. As the angle of attack increases to 3° (b), stronger velocity gradients appear along the suction side, and the first small vortices begin to form near the trailing edge, indicating the onset of flow separation. At 6° (c), these vortices grow in size and intensity, producing a distinct low-velocity region above the upper surface, which increases drag while still sustaining lift. By 9° (d), the separated region expands significantly, and the airflow streamlines clearly show strong vortices along the suction side, characteristic of stall conditions.

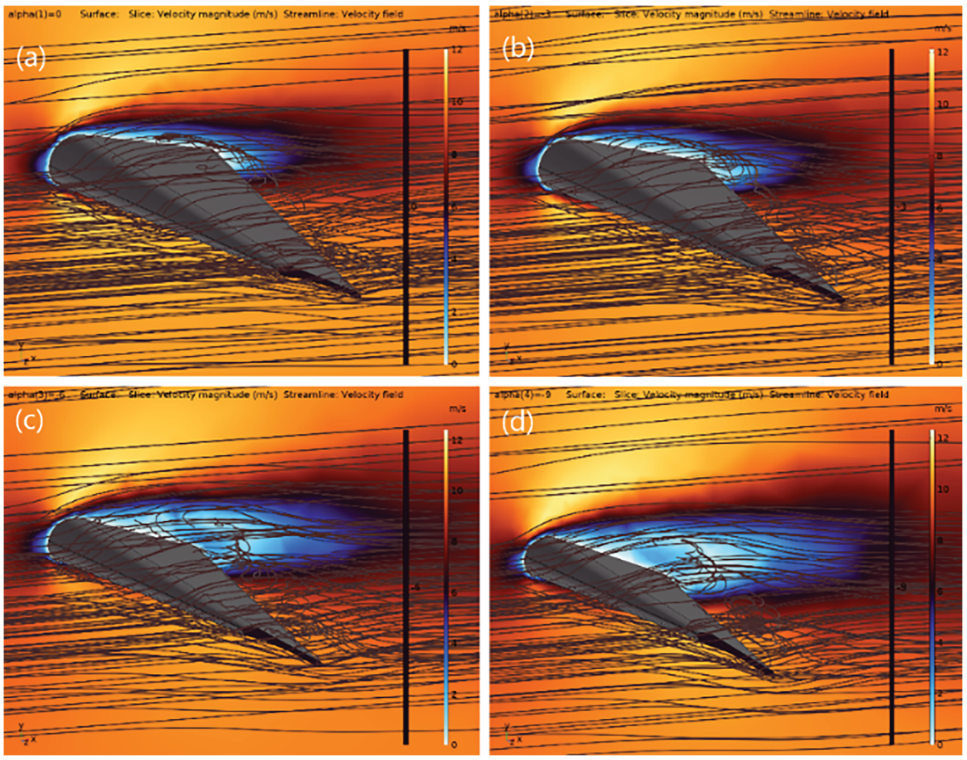

Figure 17: Velocity fields and airflow streamlines around the blade at angles of attack (**a**) 0°, (**b**) 3°, (**c**) 6°, and (**d**) 9°, illustrating the transition from attached flow at low incidence to vortex-dominated separation at higher angles.

The figure also reveals that vortex structures are more pronounced near the blade tip than at the root. This is a direct consequence of the 20° twist applied along the blade span, which increases the effective angle of attack at the tip relative to the base. Consequently, even when the nominal angle of attack for the entire blade is relatively small, the tip section operates at much higher local angles, promoting earlier vortex formation and flow separation. This explains why stall typically initiates at the blade tip and then propagates inward. For this reason, when the same airfoil design is modeled in two dimensions where the angle of attack is uniform along the chord the effective stall angle is observed to reach about 14° as shown in Fig. 18, highlighting the contrast between 2D and 3D aerodynamic behavior in twisted blades.

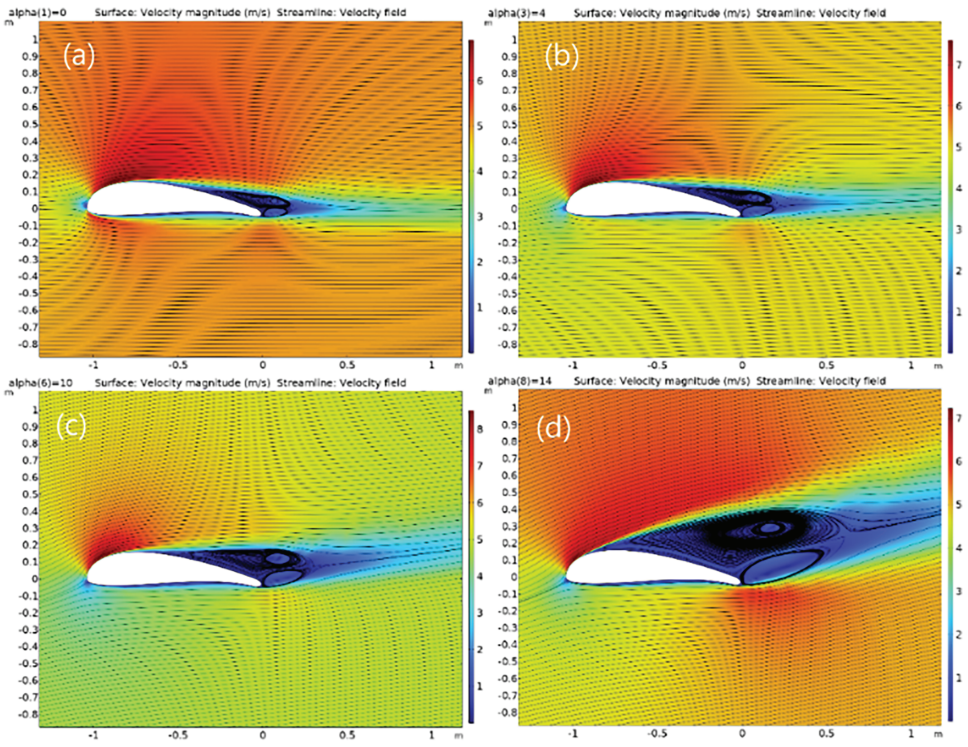

Figure 18: Velocity fields and streamline patterns around the airfoil at angles of attack of (**a**) 0°, (**b**) 4°, (**c**) 10°, and (**d**) 14°.

The velocity fields and streamline patterns around the airfoil at low incidence (a), flow remains fully attached with smooth streamlines. Increasing the angle of attack (b–c) accelerates flow over the upper surface and begins to form trailing-edge vortices, signaling the onset of separation.

At 14° (d), a large recirculation zone dominates the upper surface, with pronounced vortex structures indicating severe flow separation and stall conditions. To further quantify the aerodynamic characteristics of the blade, the lift coefficient $C_L$was computed as a function of the angle of attack. This was achieved in COMSOL Multiphysics by applying the governing aerodynamic relations (Eqs. (6) and (7)), which incorporate the integrated surface pressure forces over the blade area and the freestream velocity.

For this study, the inlet flow velocity was set to $5\,m/s$, a representative value for normal operating wind conditions [60]. By systematically varying the angle of attack from 0^o upward until the solver failed to converge or yielded unrealistic results, the lift characteristics of the designed blade were established.

The results presented in Fig. 18 illustrate the lift coefficient, C_L, as a function of angle of attack α for the DU 93-W-210 and FX63-137 blade profiles, comparing the present 2D and 3D COMSOL simulations with multiple published benchmark datasets. Over the pre-stall regime, beginning at 2° angle of attack, both COMSOL predictions exhibit a near-linear increase in lift and show good agreement with the benchmark data, indicating that the flow remains predominantly attached and that the numerical setup accurately captures the aerodynamic response in this range.

As the angle of attack increases, nonlinear effects become more pronounced, particularly for the FX63-137 profile, with the lift curves reflecting the influence of stronger adverse pressure gradients and increasing upper-surface velocity gradients. The 2D COMSOL results generally predict slightly higher lift

values than the 3D simulations, which is expected due to the absence of three-dimensional effects such as tip-induced losses.

The maximum lift coefficient is observed between approximately 8° and 15° for the both blades, followed by a marked reduction in lift, signaling the onset of stall associated with large-scale flow separation. This behavior is consistent with the trends observed in the benchmark data and aligns with the flow-visualization results discussed earlier, where the formation of separated vortical structures was evident at higher angles of attack.

Moreover, the results highlight the interplay between blade geometry and twist: although the nominal angle of attack for the blade is relatively small, the effective incidence near the tip is much higher, explaining why vortex formation and stall initiation occur in that region first. Together, these findings demonstrate that the aerodynamic performance of the proposed blade is consistent with established airfoil theory and experimental benchmarks, thereby providing confidence in the accuracy of the simulation framework for assessing lift, drag, and stall characteristics.

The progression of these flow patterns closely agrees with the lift curve Fig. 19, where lift increases with angle of attack until reaching a maximum before declining sharply as stall occurs.

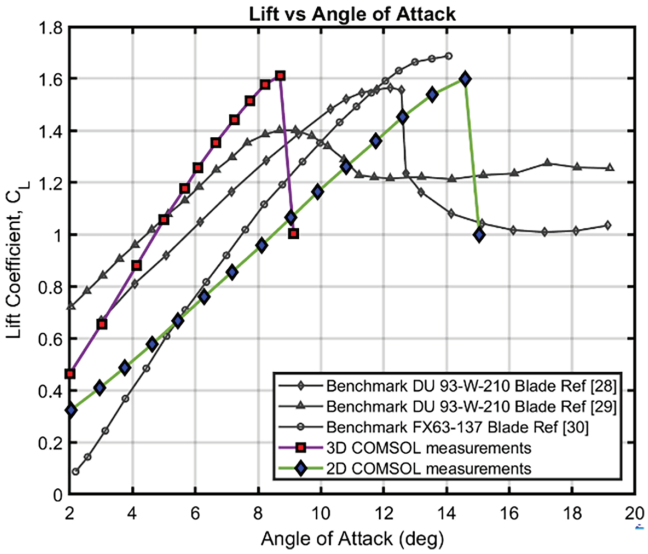

Figure 19: Computed lift coefficient as a function of angle of attack compared with published benchmark data.

The agreement between the streamline visualizations, vortex dynamics, and the $C_L - \alpha$ curve strongly validates the accuracy of the COMSOL model while reinforcing classical aerodynamic theory and published findings on stall behavior in twisted blades.

4.5 Nanocomposite Material Integration and Structural Performance Analysis

Beyond geometric optimization and structural reinforcement, material selection plays a crucial role in maximizing the performance and durability of wind turbine blades. In this research, advanced nanocomposite materials, including CNTs, nano-silica, and hybrid nanocomposites, are incorporated into the composite laminate structure of the blade. Table 1. Presents the key mechanical parameters, such as Young's modulus, tensile strength, density, and Poisson's ratio of the nanocomposite materials employed in the structural simulations.

Table 1: Mechanical properties of nanocomposite materials used in the wind turbine blade model.

Property	Carbon Nanotubes (CNTs)	Nano-Silica	Hybrid Nanocomposites
Young's Modulus (GPa)	1000–1300	50–80	10–50
Tensile Strength (GPa)	50–150	2–10	5–20
Shear Modulus (GPa)	200–600	20–35	5–20
Density (g/cm^3)	1.3–1.4	2.2–2.5	1.5
Poisson's Ratio	0.15–0.28	0.17–0.22	0.2–0.35

To accurately model the proposed reinforcement concept, both the conventional and diamond-lattice blade geometries were reconstructed within COMSOL Multiphysics® using the built-in CAD tools and the Equivalent Single Layer (ESL) laminate theory. This approach enabled the creation of a detailed 3D shell representation of the blade, capturing the interaction between the structural shell and the internal lattice framework. The diamond reinforcement was embedded directly into the shell model by integrating interconnected longitudinal, diagonal, and cross-bracing members, allowing the load transfer pathways of the lattice to be fully represented in the finite element mesh. The composite blade layup was defined using ten layers, each with a thickness of 10 mm, to represent the nano-enhanced material system. Material models for CNT-reinforced, nano-silica–reinforced, and hybrid nanocomposite laminates were assigned on a layer-by-layer basis to reflect their stiffness, strength, and damping characteristics.

The incorporation of nanomaterials markedly improves the weight-to-strength ratio, resulting in a lighter yet stronger blade capable of withstanding the combined aerodynamic, centrifugal, and gravitational loads typical of operational conditions. The addition of CNTs within the resin matrix enhances interlaminar bonding between fiber layers and significantly increases vibration damping, reducing resonance effects that can accelerate fatigue damage. As a result, CNT-reinforced composites are particularly advantageous for minimizing long-term deflection and maintaining blade stiffness under cyclic wind loading. To accurately represent the layered configuration of the composite material, the blade structure is modeled using the Equivalent Single Layer (ESL) theory, which allows for efficient numerical treatment of multiple laminae while preserving their overall stiffness and strength characteristics.

To assess the structural response of wind turbine blades fabricated from different nanocomposite materials, finite element simulations were conducted under realistic operating conditions. Each blade was subjected to a combined loading case consisting of gravity and centrifugal forces, representing typical steady-state conditions encountered during turbine operation.

As illustrated in Fig. 20, three blade configurations were analyzed: the top blade reinforced with nano-silica, the middle blade reinforced with CNTs, and the bottom blade reinforced with hybrid nanocomposites. All blades are modeled as laminated composite structures composed of carbon–epoxy, glass–vinylester, and PVC foam core materials. Due to the large number of layers, the composite laminates were simplified using the ESL theory, which preserves the global stiffness and deformation behavior of the multi-layered composite. The color contours in the figure represent the von Mises stress distribution (N/m^2), revealing the intensity and spatial variation of stresses across each blade.

Among the three materials, the CNT-reinforced blade exhibits the lowest stress magnitudes and a more uniform stress gradient, particularly near the root and spar regions where maximum loads typically occur. This indicates a superior load-bearing capacity, enhanced fatigue resistance, and improved vibration damping compared to the nano-silica and hybrid nanocomposite blades.

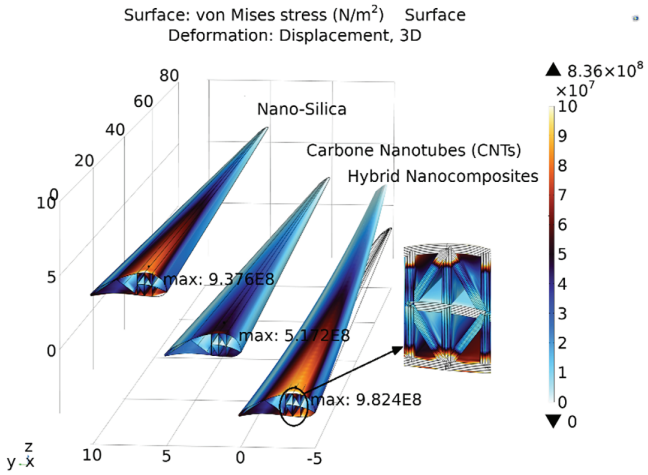

Figure 20: Comparative von Mises stress distribution for wind turbine blades fabricated from different nanocomposite materials under combined gravity and centrifugal loading.

Furthermore, the inclusion of CNTs within the composite matrix enhances interlaminar bonding and damping efficiency, leading to smoother stress transitions and reduced strain peaks throughout the structure. Consequently, CNT-reinforced laminates contribute to a longer service life, lower maintenance requirements, and greater operational reliability in wind turbine blade applications.

A zoomed schematic (Fig. 20) has been added to illustrate how the multilayer nanomaterial system and the internal diamond structure were integrated into the blade shell, ensuring that both geometric and material innovations were fully captured in the simulation workflow.

Compared with other nanofillers like nano-silica and hybrid composites, CNTs achieved the best balance of stiffness, strength, and energy absorption, ensuring greater structural and aerodynamic stability.

The redesigned blade incorporating CNT-reinforced materials and optimized internal supports showed a 44.83%–47.35% as it compared to nano-silica and hybrid composites decrease in peak stress, demonstrating enhanced resistance to deformation, fatigue, and delamination especially in critical zones such as the root and spar caps.

4.6 Comparative Analysis of Conventional and Proposed Blade Designs

To accurately model the proposed reinforcement concept, both the conventional and diamond-lattice blade geometries were reconstructed within COMSOL Multiphysics® using the built-in CAD tools and the ESL laminate theory. This approach enabled the creation of a detailed 3D shell representation of the blade, capturing the interaction between the structural shell and the internal lattice framework. The diamond reinforcement was embedded directly into the shell model by integrating interconnected longitudinal, diagonal, and cross-bracing members, allowing the load transfer pathways of the lattice to be fully represented in the finite element mesh. The composite blade layup was defined using ten layers, each with a thickness of 10 mm, to represent the nano-enhanced material system. Material models for CNT-reinforced, nano-silica–reinforced, and hybrid nanocomposite laminates were assigned on a layer-by-layer basis to reflect their stiffness, strength, and damping characteristics.

To evaluate the structural improvements achieved through internal reinforcement and material optimization, both the conventional and proposed wind turbine blade designs were modeled using CNT-reinforced composite material. CNTs were selected for both models as this nanocomposite demonstrated the

best mechanical performance among all materials tested, exhibiting superior handling of stress, strain, and fatigue compared to nano-silica and hybrid nanocomposites.

As shown in Fig. 21, the simulation results under combined gravity and centrifugal loading reveal a clear performance enhancement in the proposed blade design.

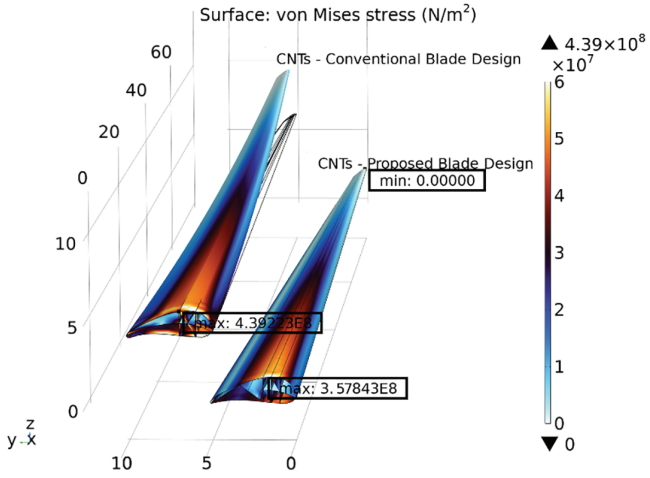

Figure 21: Comparison of von Mises stress distribution between the conventional and proposed CNT-reinforced wind turbine blade designs.

The new configuration demonstrates a 18.53% reduction in peak von Mises stress relative to the conventional model, along with a more uniform stress distribution along the span. This improvement indicates a significant increase in structural stiffness and fatigue resistance, especially near the root and spar junctions where mechanical loads are concentrated.

The reduction in stress concentration suggests that the proposed design provides more efficient load transfer and energy dissipation, leading to lower deformation amplitudes and extended service life. The integration of CNTs amplifies these benefits by enhancing interlaminar bonding and vibration damping, which together contribute to a stronger, lighter, and more durable blade suitable for long-term operation under variable wind conditions.

Figs. 20 and 21 reveal that material selection and structural optimization significantly enhance the mechanical performance of wind turbine blades. The use of CNT-reinforced nanocomposites led to notable reductions in stress and improved fatigue resistance compared to conventional composites. CNT-based laminates exhibited the lowest von Mises stress and the most uniform stress distribution, confirming their superior load transfer and vibration damping properties.

4.7 Dynamic Analysis Using Campbell Diagram

A Campbell diagram is an essential diagnostic tool in the study of rotating machinery, providing valuable insight into the vibration characteristics and resonance behavior of turbine blades. It graphically represents the relationship between the rotational speed (RPM) and the natural frequencies of the structure, thereby identifying potential resonance zones where excitation frequencies coincide with the system's natural frequencies. The excitation frequency acting on the rotating blade is determined by the expression:

$$f_{exc} = n \cdot f_{rotor} = n \cdot \frac{N}{60} \tag{10}$$

where f_{exc} denotes the excitation frequency in hertz, f_{rotor} is the rotational frequency, N is the rotational speed in revolutions per minute, and n represents the harmonic order $1x, 2x, 3x$ etc., corresponding to the number of excitations occurring per revolution.

Fig. 22a,b, presents the Campbell diagram for the CNT-reinforced wind turbine blade and its corresponding Discrete Fourier Transform (DFT) frequency spectrum respectively. Fig. 22a, shows how the blade's natural frequencies evolve with increasing rotational speed, with each curve representing a distinct vibration mode, such as flapwise bending, edgewise bending, and torsional response. The slight upward trend in these curves reflects centrifugal stiffening, where rotation increases the effective stiffness of the blade and elevates its natural frequencies as RPM increases. Diagonal lines represent harmonic excitation frequencies; intersections between these lines and the natural frequency curves would indicate resonance. However, no such intersections occur within the turbine's operating range, confirming that the blade avoids resonance conditions and maintains stable dynamic behavior.

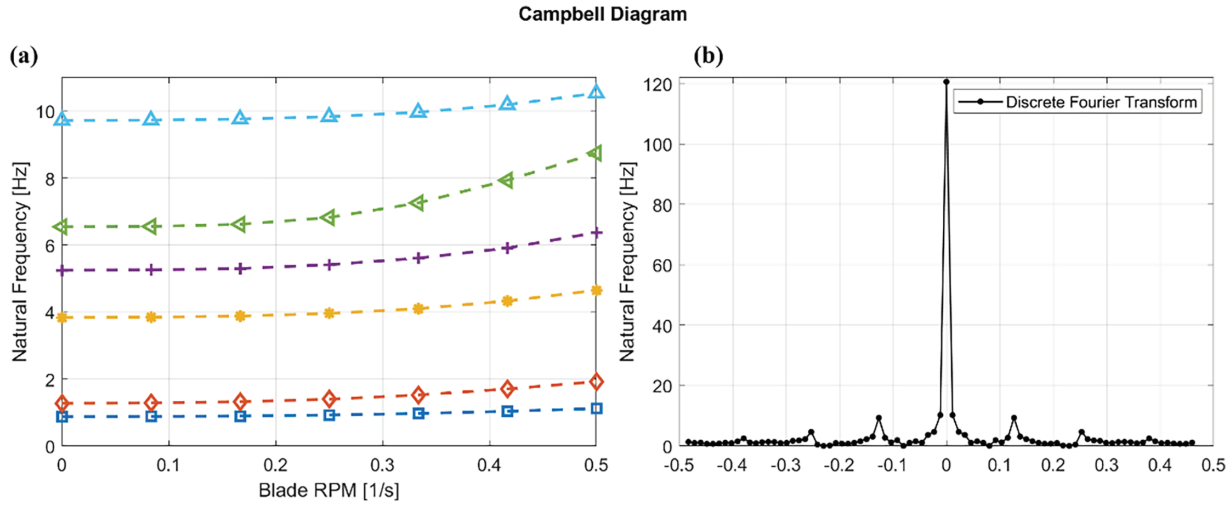

Figure 22: (**a**) Campbell diagram showing the variation of blade natural frequencies with rotational speed and (**b**) the corresponding DFT-based frequency response. The absence of intersections between excitation peaks and natural modes within the operating range indicates stable dynamic behavior and no resonance risk.

Fig. 22b, illustrates the simulated vibration response obtained through the DFT, which plots frequency (Hz) along both axes to show the relationship between excitation and response frequencies.

The dominant peak at the center of the spectrum corresponds to the primary excitation frequency, representing the fundamental rotational speed of the turbine. Smaller, symmetrically distributed side peaks correspond to higher-order harmonics generated by periodic aerodynamic loading effects, such as 1P blade-passing frequency, tower-shadow interaction, and gravitational imbalances. The strong central spike indicates a major periodic component, while the surrounding peaks confirm harmonic coupling between structural vibration modes and rotational excitations.

This Campbell-type representation is especially important for validating the absence of resonance throughout the turbine's operational envelope. The clear separation between excitation peaks and modal frequencies demonstrates that the proposed diamond-lattice internal structure and CNT-reinforced composite system provide enhanced dynamic stability, reduced susceptibility to modal coupling, and improved damping behavior. The absence of frequency overlap or significant amplification of harmonic response

indicates smoother operational behavior, lower vibration transmission, and reduced fatigue loading on the blade.

Overall, the combined Campbell diagram and DFT analysis substantiate the mechanical robustness and dynamic efficiency of the proposed blade configuration. The results confirm that the CNT-reinforced diamond-lattice blade experiences no resonance risk within its operational speed range, supporting improved structural reliability, enhanced fatigue performance, and extended service life under realistic wind turbine loading conditions.

5 Conclusion

This study introduced a new wind turbine blade architecture incorporating an optimized diamond-lattice internal reinforcement designed to improve structural efficiency and load transfer. Finite element simulations in COMSOL Multiphysics® demonstrated that the proposed lattice framework reduces the peak von Mises stress by 11.38%, achieves an approximate 15.39% reduction in volumetric elastic strain, increases fatigue performance by 14.38%, and provides a substantial improvement in buckling resistance compared with the conventional X-shaped design. These results confirm that the lattice geometry creates a significantly more effective load-carrying structure, particularly in high-stress regions such as the root and spar caps.

Nano-enhanced materials were also evaluated to complement the structural concept. Although CNT-reinforced laminates offered additional gains in stiffness-to-weight performance, vibration damping, and strain uniformity, the primary performance improvements were driven by the optimized internal structural layout. Dynamic analysis through Campbell diagrams validated that the redesigned blade operates safely below resonance conditions, with natural frequencies shifting upward due to centrifugal stiffening, further supporting its stability across the operational speed range.

In summary, the major contribution of this research is the development and validation of a diamond-lattice internal reinforcement that measurably enhances mechanical performance without increasing mass or compromising manufacturability. By achieving higher stiffness, improved fatigue resistance, and better stability under aerodynamic, gravitational, and centrifugal loads, the proposed design provides a promising pathway toward lighter, stronger, and longer-lasting blades for next-generation wind energy systems. Future work will involve experimental validation, improved aeroelastic coupling, and assessment of large-scale manufacturability to advance practical deployment.

Acknowledgement: Not applicable.

Funding Statement: The authors received no specific funding.

Author Contributions: Mohammed Yahya developed the primary research concept, designed the study, performed the analysis, and prepared the manuscript. Joban Sahota, Gursingh Aikum Dhugga, and Saiakash Shunmugavel, the author's undergraduate mechanical engineering students, assisted with gathering reference materials, supporting the literature review, and participating in running and observing the COMSOL Multiphysics simulations. Safaaldeen A. Sulyman provided technical guidance and valuable suggestions related to the COMSOL simulation setup and modeling approach. All authors reviewed and approved the final version of the manuscript.

Availability of Data and Materials: All data and supporting materials used in this study are included in the manuscript and are also available from the corresponding author upon reasonable request.

Ethics Approval: This study did not involve human participants, animals, or sensitive data, and therefore did not require ethics approval.

Conflicts of Interest: The authors declare no conflicts of interest.

Appendix A Matlab Verification of Cantilever Box Beam

This appendix presents a hand calculation implemented in Matlab®, used to verify the structural response of a tapered cantilever steel box beam subjected to a uniformly distributed load. The objective of the calculation is to determine the fixed-end bending stress and the volumetric elastic strain using classical beam theory and to provide an independent verification benchmark for numerical or finite-element results. The beam is modeled as a single-cell rectangular box section with linearly varying outer dimensions and wall thickness along its span. Linear elastic material behavior is assumed.

A cantilever beam of length $L = 80$ m, fixed at $x = 0$ and free at $x = L$, is made of a nanotube composite material with an elastic modulus of $E = 1000$ GPa. The beam has a linearly varying rectangular cross-section: the width decreases from $b_o = 8$ m at the fixed end to $b_L = 2.4$ m at the free end, and the thickness decreases from $t_0 = 0.5$ m to $t_L = 0.15$ m. The beam is subjected to a total vertical load $W = 200$ kN. The simple beam verification against the proposed configuration was performed using the MATLAB implementation presented below (Listing 1).

Listing 1: Tapered cantilever box beam with two internal webs.

```
% Cross-section model:
%       - Outer rectangular box (walls thickness t(x))
%       - Two INTERNAL vertical webs (plates parallel to h)
% Total I(x) computed by parallel-axis theorem:
%     I_total = I_box + sum(I_web_local + A_web * y_bar^2)
% ————————————————————————————————————-
close all; clear; clc;
%% ————————– INPUTS ————————————————–
% Span
L     = 80.0;                  % m
% Outer dimensions (linear taper)
b0 = 8.0; bL = 2.4;      % outer width (m)
h0 = 4.0; hL = 0.5;      % outer depth (m)
% Box wall thickness (linear taper)
t0 = 0.50; tL = 0.15;      % m
% Internal web thicknesses (linear taper)
tv0 = 0.30; tvL = 0.10;        % vertical web thickness (m)
th0 = 0.30; thL = 0.10;        % horizontal web thickness (m)
% Material
E = 1000e9;                    % Pa
% Loading
W_total = 200e3;               % N (200 kN total)
w = W_total / L;               % N/m
% Discretization
N = 20001;
x = linspace(0, L, N);
%% ————————– DEFINE WEB LAYOUT ————————————-
% two vertical webs and one horizontal location
vertical_web_xi            = [0.23,0.475];
```

```
horizontal_web_eta = [];
%% ———————————— TAPERED FUNCTIONS ————————————————
linTaper = @(x, y0, yL) (y0 + (yL - y0) .* (x ./ L));
b  = linTaper(x, b0, bL);
h  = linTaper(x, h0, hL);
t  = linTaper(x, t0, tL);
tv = linTaper(x, tv0, tvL);
th = linTaper(x, th0, thL);
% Inner void dimensions
bi = max(b - 2.*t, 0);
hi = max(h - 2.*t, 0);
%% ———————————— SECTION I(x) ————————————————————
% 1) Box contribution (strong axis)
I_box = (b .* h.^3 - bi .* hi.^3) ./ 12;
% 2) Internal vertical webs contribution
% Assumption: vertical webs span the full inner height hi(x)
% Their centroid is at y=0 (neutral axis), so no A*y^2 term.
I_v_total = zeros(size(x));
for k = 1:numel(vertical_web_xi)
    % Local I of a vertical plate about the NA (strong axis):
    % I_local = (t * h^3)/12
    I_local = (tv .* hi.^3) ./ 12;
    I_v_total = I_v_total + I_local;
end
% 3) Internal horizontal webs contribution
% Assumption: horizontal webs span the full inner width bi(x)
% Their centroid is at y = (eta-0.5)*hi(x), so A*y^2 term is critical.
I_h_total = zeros(size(x));
for k = 1:numel(horizontal_web_eta)
    eta = horizontal_web_eta(k);
    % Plate area
    A_web = th .* bi;                          % A = thickness * width
    % Vertical centroid offset from neutral axis (y=0 at section mid-height)
    y_bar = (eta - 0.5) .* hi;                 % m
    % Local I of a horizontal plate about its own centroid axis
    % Plate dims: width = bi, thickness = th (vertical thickness)
    % For strong-axis bending, thickness is in vertical direction:
    I_local = (bi .* th.^3) ./ 12;
    % Parallel-axis contribution
    I_h_total = I_h_total + (I_local + A_web .* y_bar.^2);
end
% Total I(x)
I = I_box + I_v_total + I_h_total;
%% ———————————— FIXED-END ACTIONS ————————————————
```

```
V0 = w * L;
M0 = w * L^2 / 2;
%% ———————— FIXED-END STRESS/STRAIN ————————-
I0 = I(1);
c0 = h0 / 2;
S0 = I0 / c0;
sigma_max          = M0 / S0;              % Pa
epsilon_max = sigma_max / E;
% Curvature check
kappa0 = M0 / (E * I0);
epsilon_kappa = kappa0 * c0;
 %% ———————— PRINT RESULTS ————————————————-
fprintf('\n— Tapered cantilever stiffened box (two webs) —\n');
fprintf('W_total                                = %.3f kN\n', W_total/1e3);
fprintf('w                                        = %.6f kN/m\n', w/1e3);
fprintf('\n');
fprintf('sigma_max                          = %.6f MPa\n', sigma_max/1e6);
fprintf('epsilon_max                       = %.12e\n', epsilon_max);
fprintf('epsilon_kappa (check)          = %.12e\n', epsilon_kappa);
fprintf('\n');
%% ———————— OPTIONAL PLOTS ————————————————
figure; plot(x, I, 'LineWidth', 1.5); grid on;
xlabel('x (m)'); ylabel('I(x) (m^4)');
title('Bending stiffness I(x) along span');
— Tapered cantilever stiffened box (two webs) —
sigma_max                          = 0.566038 MPa
epsilon_max                       = 5.660377358491e-07
epsilon_kappa (check)       = 5.660377358491e-07
```

Appendix B Mesh Convergence Study

A mesh convergence study was performed to ensure that the finite element results are independent of spatial discretization. The study was carried out using a representative blade configuration subjected to the same material properties, boundary conditions, and loading conditions as those employed in the main structural analysis.

Three mesh levels, coarse, normal, and finer, were generated using a consistent meshing strategy and element formulation. Mesh refinement was applied systematically, with increased element density introduced primarily in regions of high stress gradients near the blade root. The geometric representation and element type were kept identical across all mesh levels to isolate the effect of mesh density on the numerical results.

For each mesh, the maximum von Mises stress and the volumetric elastic strain were extracted, as these response quantities are sensitive to mesh resolution and are directly relevant to the structural performance assessment. Results were evaluated for the proposed blade configuration, and a simplified beam representation. The numerical values obtained from the convergence study are summarized in Table A1.

Table A1: Mesh convergence results for the representative blade model.

Mesh level	Number of Elements	Maximum von Mises Stress (MPa)		Volumetric Elastic Strain × 10^{-7}	
		Prop. Beam	Simple Beam	Prop. Beam	Simple Beam
Coarse	31,711 domain 10,796 boundary 1586 edge	0.41985	0.53113	6.19735	6.32875
Normal	42,010 domain 18,054 boundary 2307 edge	0.42017	0.53118	6.09759	6.07752
Finer	578,007 domain 242,668 boundary 8077 edge	0.42387	0.53865	6.04922	6.15557

As the mesh is refined from coarse to finer, the predicted von Mises stress values increase slightly and converge toward stable solutions for all three structural representations. For the simplified beam model, the maximum von Mises stress increases from 0.53113 MPa in the coarse mesh to 0.53865 MPa in the finer mesh, corresponding to a relative variation of 1.4%. In comparison, the proposed configuration exhibits a smaller increase from 0.41985 to 0.42387 MPa, resulting in a relative variation of 1%. A similar convergence trend is observed for the volumetric elastic strain, indicating reduced sensitivity to mesh refinement.

A comparable convergence behavior is also observed for the blade volumetric elastic strain, further demonstrating diminishing sensitivity of this response quantity to mesh density. For the simplified beam model, the maximum volumetric elastic strain decreases from 6.32875×10^{-7} in the coarse mesh to 6.15557×10^{-7} in the finer mesh, corresponding to a relative variation of 2.73%. Likewise, for the proposed configuration, the volumetric elastic strain decreases from 6.19735×10^{-7} to 6.04922×10^{-7}, yielding a comparable variation of 2.4%.

The von Mises stress and volumetric elastic strain distributions obtained using the coarse mesh are presented in Fig. A1, while the corresponding results for the finer mesh are shown in Fig. A2. In both cases, the simplified beam model exhibits peak stress and strain concentrations near the blade root, where bending moments are highest, with magnitudes gradually decreasing toward the free end of the blade. The volumetric elastic strain fields follow a similar spatial trend.

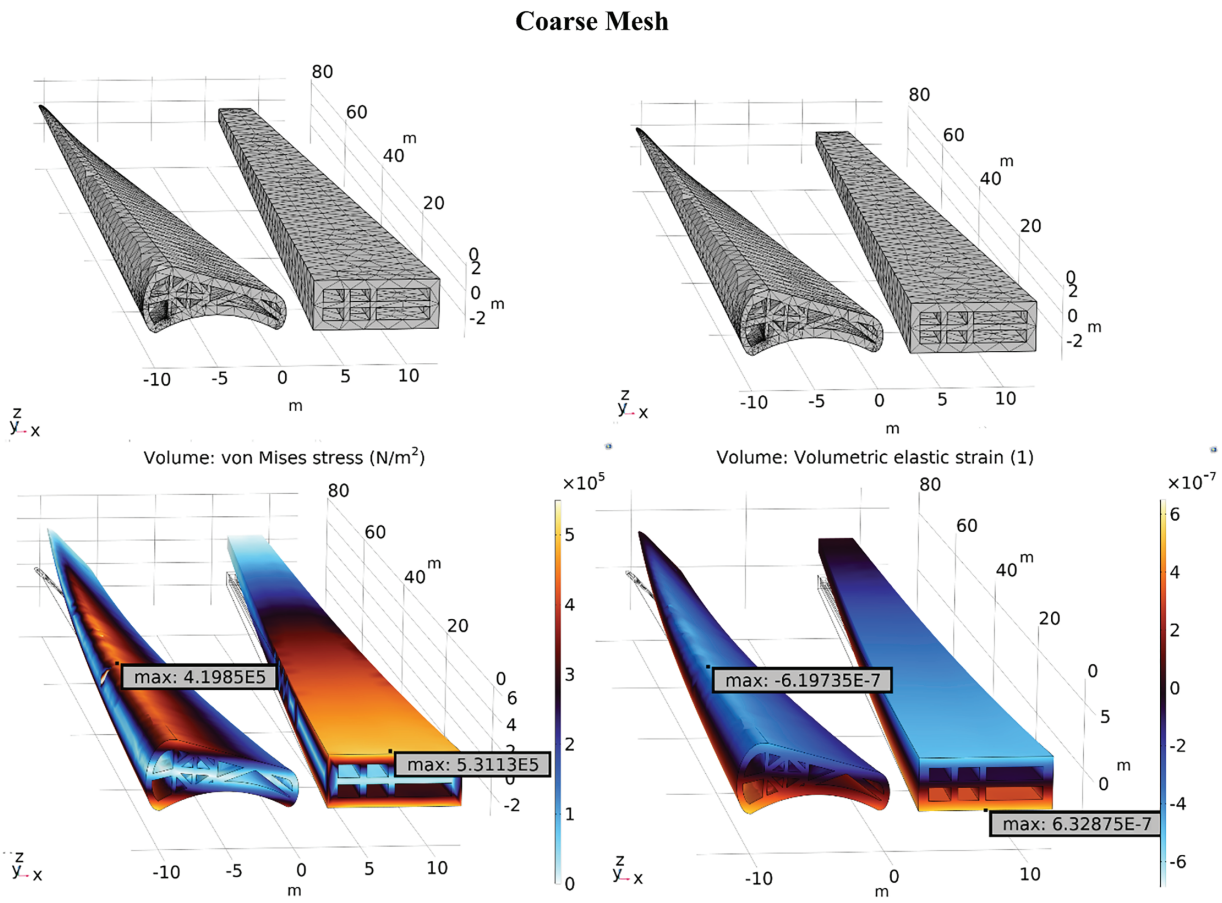

Figure A1: Finite element mesh and von Mises stress distribution for the representative blade model using the coarse mesh. Peak stresses are localized near the blade root, with stress magnitude decreasing smoothly toward the free end.

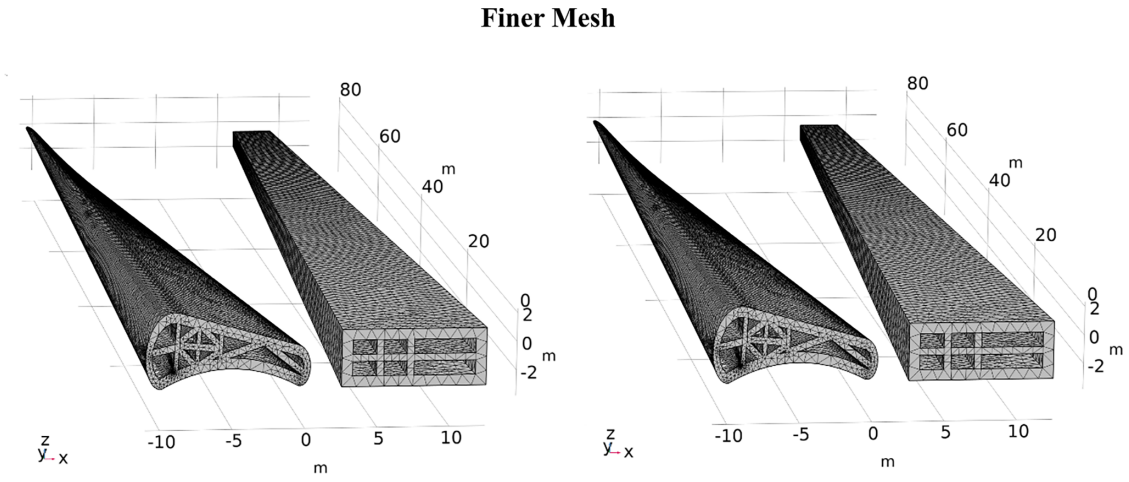

Figure A2: (Continued)

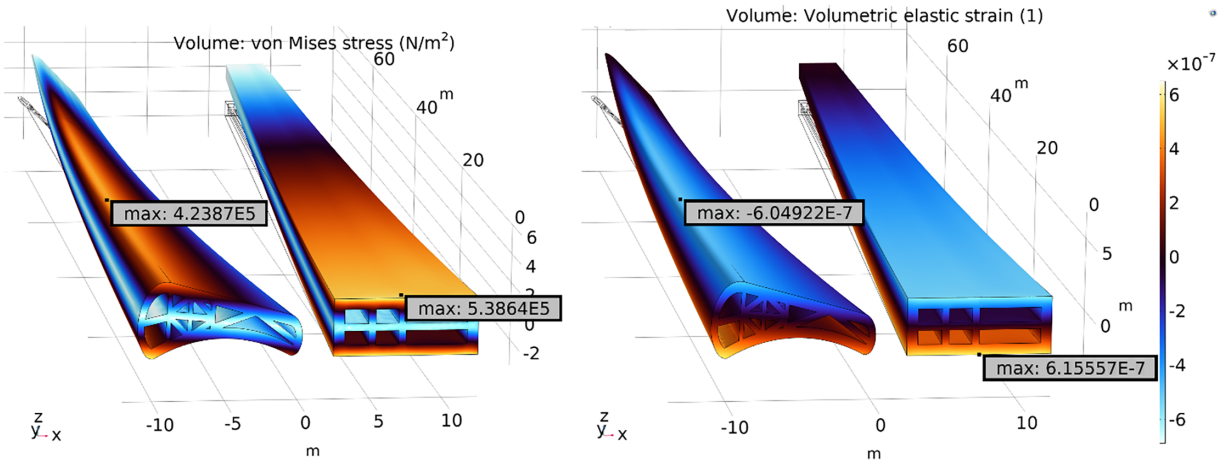

Figure A2: von Mises stress and volumetric elastic strain distributions for the simplified cantilever beam obtained using the fine finite element mesh.

In contrast, for the proposed configuration, the maximum stress and strain are observed closer to the mid-span region of the blade. This behavior is attributed to the increased geometric and structural complexity of the proposed design, including internal stiffening features and nonuniform load transfer paths, which redistribute stresses and strains away from the root region when compared with the simplified beam model. Despite these differences in localization, the overall stress and strain distributions remain consistent across mesh levels, confirming the convergence and numerical stability of the finite element solution.

The observed variations in stress and strain, on the order of approximately 1%–3%, are considered acceptable for structural finite element analysis of complex geometries, as they primarily result from improved resolution of localized stress and strain gradients rather than changes in the global structural response. Moreover, the monotonic convergence behavior and consistent spatial distributions confirm that the numerical solutions are sufficiently mesh-independent for comparative design evaluation and parametric studies.

References

1. Price TJ. James blyth—britain's first modern wind power pioneer. Wind Eng. 2005;29(3):191–200. doi:10.1260/030952405774354921.
2. Thomas L, Ramachandra M. Advanced materials for wind turbine blade—a review. Mater Today Proc. 2018;5(1):2635–40. doi:10.1016/j.matpr.2018.01.043.
3. Jamieson P. Innovation in wind turbine design. Hoboken, NJ, USA: John Wiley & Sons, Inc.; 2018. doi:10.1002/9781119137924.
4. Sørensen JN. General momentum theory for horizontal axis wind turbines. Berlin/Heidelberg, Germany: Springer; 2016. doi:10.1007/978-3-319-22114-4.
5. Hau E, von Renouard H. Wind turbines: fundamentals, technologies, application, economics. Berlin/Heidelberg, Germany: Springer; 2006. doi:10.1007/3-540-29284-5.
6. Brondsted P, Nijssen RP, Goutianos S. Advances in wind turbine blade design and materials. Cambridge, UK: Woodhead Publishing; 2023.
7. Schubel PJ, Crossley RJ. Wind turbine blade design review. Wind Eng. 2012;36(4):365–88. doi:10.1260/0309-524x.36.4.365.
8. Balat M. A review of modern wind turbine technology. Energy Sources Part A Recovery Util Environ Eff. 2009;31(17):1561–72. doi:10.1080/15567030802094045.

9. Rehman S, Alam M, Alhems L, Rafique M. Horizontal axis wind turbine blade design methodologies for efficiency enhancement—a review. Energies. 2018;11(3):506. doi:10.3390/en11030506.
10. Martulli LM, Diani M, Sabetta G, Bontumasi S, Colledani M, Bernasconi A. Critical review of current wind turbine blades' design and materials and their influence on the end-of-life management of wind turbines. Eng Struct. 2025;327:119625. doi:10.1016/j.engstruct.2025.119625.
11. Richards PW, Griffith DT, Hodges DH. Aeroelastic design of large wind turbine blades considering damage tolerance. Wind Energy. 2016;20(1):159–70. doi:10.1002/we.1997.
12. Wu S, Cai C, Zhang L, Hu Z, Sun X, Zhong X, et al. Optimizing wind turbine blade performance: a multi-objective approach for power, load and stall characteristics. Energy. 2025;331:136871. doi:10.1016/j.energy.2025.136871.
13. de Almeida IT, Lapa GVP, Gay Neto A, de Almeida SFM. Design and extreme structural analysis of wind turbine blades: beam and shell model comparison and discussion for a 10-MW reference turbine. Eng Struct. 2025;334:120155. doi:10.1016/j.engstruct.2025.120155.
14. Zhu H, Miao W, Wang H, Li C, Fan S, Yue M. Structural design and performance anaylsis of wind turbine blades based on bionics. J Mech Strength. 2025;47(4):112–21.
15. Agarwala R, Chin RA. Structural design and analysis of a redesigned wind turbine blade. Int J Ambient Energy. 2022;43(1):1895–901. doi:10.1080/01430750.2020.1723688.
16. Taima MS, El-Sayed TA, Friswell MI. Dynamic stability analysis of tapered rotating beams with 2D functionally graded materials: a comparative study of Floquet theory approaches. Thin Walled Struct. 2025;213(1):113257. doi:10.1016/j.tws.2025.113257.
17. Capuzzi M, Pirrera A, Weaver PM. Structural design of a novel aeroelastically tailored wind turbine blade. Thin Walled Struct. 2015;95:7–15. doi:10.1016/j.tws.2015.06.006.
18. Migliaccio G, Ruta G. Rotor blades as curved, twisted and tapered beam-like structures subjected to large deflections. Eng Struct. 2020;222:111089. doi:10.1016/j.engstruct.2020.111089.
19. Burton T, Jenkins N, Sharpe D, Bossanyi E. Wind energy handbook. 2nd ed. Chichester, UK: Wiley; 2011.
20. Manwell JF, McGowan JG, Rogers AL. Wind energy explained: theory, design and application. Hoboken, NJ, USA: John Wiley & Sons, Inc.; 2009. doi:10.1002/9781119994367.
21. Overgaard LCT, Lund E, Thomsen OT. Structural collapse of a wind turbine blade. Part A: static test and equivalent single layered models. Compos Part A Appl Sci Manuf. 2010;41(2):257–70. doi:10.1016/j.compositesa.2009.10.011.
22. Overgaard LCT, Lund E. Structural collapse of a wind turbine blade. Part B: progressive interlaminar failure models. Compos Part A Appl Sci Manuf. 2010;41:271–83. doi:10.1016/j.compositesa.2009.10.012.
23. Jensen FM, Arconada JO, Werk M, Berggreen C, Sørensen JD, Zhong G, et al. Torsional effects on wind turbine blades and impact on field damages. IOP Conf Ser Mater Sci Eng. 2023;1293(1):012005. doi:10.1088/1757-899x/1293/1/012005.
24. Alam K, Ullah H, Iqbal M, Husain A, Rasul A, Iqbal M. Structural integrity of offshore wind turbine blade under extreme gust and normal operating conditions. Results Eng. 2025;25:104572. doi:10.1016/j.rineng.2025.104572.
25. Ashwill T. Materials and innovations for large blade structures: research opportunities in wind energy technology. In: Proceedings of the 50th AIAA/ASME/ASCE/AHS/ASC Structures, Structural Dynamics, and Materials Conference; 2009 May 4–7; Palm Springs, CA, USA. doi:10.2514/6.2009-2407.
26. Pogosyan M, Nazarov E, Bolshikh A, Koroliskii V, Turbin N, Shramko K. Aircraft composite structures integrated approach: a review. J Phys Conf Ser. 2021;1925(1):012005. doi:10.1088/1742-6596/1925/1/012005.
27. Wilson RE, Lissaman P, Walker SN. Aerodynamic performance of wind turbines. Oak Ridge, TN, USA: U.S. Department of Energy Office of Scientific and Technical Information; 1976. Report No.: 7117144.
28. Timmer WA, van Rooij RPJOM. Summary of the delft university wind turbine dedicated airfoils. J Sol Energy Eng. 2003;125(4):488–96. doi:10.1115/1.1626129.
29. Selig MS, Guglielmo JJ, Broeren AP, Giguere P. Summary of low-speed airfoil data. Ann Arbor, MI, USA: SoarTech Publications; 1995.
30. Bertagnolio F, Sørensen N, Johansen J, Fuglsang P. Wind turbine airfoil catalogue [Internet]. DTU Library. 2001. [cited 2026 Jan 26]. Available from: https://backend.orbit.dtu.dk/ws/files/7728949/ris_r_1280.pdf.
31. Ajayan PM, Tour JM. Nanotube composites. Nature. 2007;447(7148):1066–8. doi:10.1038/4471066a.

32. Vafaeva KM, Zegait R. Carbon nanotubes: revolutionizing construction materials for a sustainable future: a review. Res Eng Struct Mat. 2023;10:559–621. doi:10.17515/resm2023.42ma0818rv.
33. Fenta EW, Mebratie BA. Advancements in carbon nanotube-polymer composites: enhancing properties and applications through advanced manufacturing techniques. Heliyon. 2024;10(16):e36490. doi:10.1016/j.heliyon.2024.e36490.
34. Coleman JN, Khan U, Gun'ko YK. Mechanical reinforcement of polymers using carbon nanotubes. Adv Mater. 2006;18(6):689–706. doi:10.1002/adma.200501851.
35. Daneshvar F, Chen H, Noh K, Sue HJ. Critical challenges and advances in the carbon nanotube-metal interface for next-generation electronics. Nanoscale Adv. 2021;3(4):942–62. doi:10.1039/d0na00822b.
36. Thostenson ET, Ren Z, Chou TW. Advances in the science and technology of carbon nanotubes and their composites: a review. Compos Sci Technol. 2001;61(13):1899–912. doi:10.1016/S0266-3538(01)00094-X.
37. Pandey G, Thostenson ET. Carbon nanotube-based multifunctional polymer nanocomposites. Polym Rev. 2012;52(3):355–416. doi:10.1080/15583724.2012.703747.
38. AlTawaiha H, Alhomaidat F, Eljufout T. A review of the effect of nano-silica on the mechanical and durability properties of cementitious composites. Infrastructures. 2023;8(9):132. doi:10.3390/infrastructures8090132.
39. Uniyal P, Gaur P, Yadav J, Bhalla NA, Khan T, Junaedi H, et al. A comprehensive review on the role of nanosilica as a toughening agent for enhanced epoxy composites for aerospace applications. ACS Omega. 2025;10(16):15810–39. doi:10.1021/acsomega.4c10073.
40. Ibrahim SH, El-Tayeb NSM. Effect of nano-silica/alumina hybrid coating on erosion resistance of glass fibre-reinforced polymer for the application of wind turbine blades. Proc Inst Mech Eng Part J J Eng Tribol. 2022;236(10):2013–31. doi:10.1177/13506501211052724.
41. Dong B, Liu C, Shumuye ED, Zhang Y, Zhong H, Fang G. Effect of nano-silica on mechanical properties and microstructure of engineered geopolymer composites. Cem Concr Compos. 2025;156:105849. doi:10.1016/j.cemconcomp.2024.105849.
42. Zhang LB, Zhang HX, Liu ZJ, Jiang XY, Agathopoulos S, Deng Z, et al. Nano-silica anti-icing coatings for protecting wind-power turbine fan blades. J Colloid Interface Sci. 2023;630:1–10. doi:10.1016/j.jcis.2022.09.154.
43. Zare Y. Study of nanoparticles aggregation/agglomeration in polymer particulate nanocomposites by mechanical properties. Compos Part A Appl Sci Manuf. 2016;84:158–64. doi:10.1016/j.compositesa.2016.01.020.
44. Sharma SK, Miladinović S, Sharma LK, Gajević S, Sharma Y, Sharma M, et al. Graphene/CNT nanocomposites: processing, properties, and applications. Nanomaterials. 2026;16(2):100. doi:10.3390/nano16020100.
45. Monteiro B, Simões S. Recent advances in hybrid nanocomposites for aerospace applications. Metals. 2024;14(11):1283. doi:10.3390/met14111283.
46. Hansen MH. Modal dynamics of structures with bladed isotropic rotors and its complexity for two-bladed rotors. Wind Energ Sci. 2016;1(2):271–96. doi:10.5194/wes-1-271-2016.
47. Xu J, Zhang L, Li S, Xu J. The influence of rotation on natural frequencies of wind turbine blades with pre-bend. J Renew Sustain Energy. 2020;12(2):023303. doi:10.1063/1.5143868.
48. Hu WH, Tang DH, Wang M, Liu JL, Li ZH, Lu W, et al. Resonance monitoring of a horizontal wind turbine by strain-based automated operational modal analysis. Energies. 2020;13(3):579. doi:10.3390/en13030579.
49. Torres A, Gil J, Plaza A, Aginaga J. 4P operational harmonic and blade vibration in wind turbines: a real case study of an active yaw system and a concrete tower. Renew Energy. 2024;227:120503. doi:10.1016/j.renene.2024.120503.
50. Sedighi H, Akbarzadeh P, Salavatipour A. Aerodynamic performance enhancement of horizontal axis wind turbines by dimples on blades: numerical investigation. Energy. 2020;195(1):117056. doi:10.1016/j.energy.2020.117056.
51. Jeong JH, Ha K. Numerical investigation of three-dimensional and vortical flow phenomena to enhance the power performance of a wind turbine blade. Appl Sci. 2020;11(1):72. doi:10.3390/app11010072.
52. Wang L, Liu X, Renevier N, Stables M, Hall GM. Nonlinear aeroelastic modelling for wind turbine blades based on blade element momentum theory and geometrically exact beam theory. Energy. 2014;76:487–501. doi:10.1016/j.energy.2014.08.046.

53. Koutromanos I, McClure J. Fundamentals of finite element analysis: linear finite element analysis. Hoboken, NJ, USA: John Wiley & Sons, Inc.; 2018.
54. Fragkos PF, Theotokoglou EE. Computational analysis of a wind turbine blade for different advanced materials. Materials. 2025;18(11):2447. doi:10.3390/ma18112447.
55. Griffin DA, Ashwill TD. Blade system design studies volume I: composite technologies for large wind turbine blades. Albuquerque, NM, USA: Sandia National Laboratories; 2002.
56. Nixon-Pearson O, Greaves P, Mamalis D, Stevenson L. WP4-D1. 1. wind turbine blades design and manufacturing, current state-of-the art. Rep Corn Flow Accelarator. 2022;1–94. doi:10.1016/b978-0-08-100779-2.00006-4.
57. Mir M, Tahani M, Hassani B. Analytical prediction of Young's modulus of carbon nanotubes using a variational method. Appl Math Model. 2017;45:1031–43. doi:10.1016/j.apm.2017.01.038.
58. Hassanzadeh A, Hassanzadeh Hassanabad A, Dadvand A. Aerodynamic shape optimization and analysis of small wind turbine blades employing the Viterna approach for post-stall region. Alex Eng J. 2016;55(3):2035–43. doi:10.1016/j.aej.2016.07.008.
59. Abbott IHA, von Doenhoff AE. Theory of wing sections: including a summary of airfoil data. New York, NY, USA: Dover Publications; 1959.
60. Park J, Kim C, Dinh MC, Park M. Design of a condition monitoring system for wind turbines. Energies. 2022;15(2):464. doi:10.3390/en15020464.